# Development of Fully Interactive Hydrogen with Methane in UKESM1.0

Megan A. J. Brown[1], Nicola J. Warwick[1, 2], Nathan Luke Abraham[1, 2], Paul T. Griffiths[1, 2, 3], Steve T. Rumbold[4], Gerd A. Folberth[4], Fiona M. O'Connor[4, 5], Hannah Bryant[6], and Alex T. Archibald[1, 2]

[1]Centre for Atmospheric Science, Department of Chemistry, University of Cambridge, Cambridge, CB2 1EW, UK
[2]National Centre for Atmospheric Science (NCAS), University of Cambridge, Cambridge, CB2 1EW, UK
[3]School of Chemistry, University of Bristol, Bristol, BS8 1TS, UK
[4]Met Office Hadley Centre, Met Office, Fitzroy Road, Exeter, Devon, EX1 3PB, UK
[5]Department of Mathematics & Statistics, Global Systems Institute, University of Exeter, Exeter, EX4 4QF
[6]School of GeoSciences, University of Edinburgh, UK

**Correspondence:** Megan A. J. Brown (majb4@cam.ac.uk) and Alex T. Archibald (ata27@cam.ac.uk)

**Abstract.** Hydrogen is a potential candidate for an alternate energy source and carrier. As usage of hydrogen in industry rises, leakages into the atmosphere may occur, causing an increase in the global atmospheric hydrogen concentration. Hydrogen is an indirect greenhouse gas, known to increase methane, stratospheric water vapour, and tropospheric ozone. Methane and hydrogen are closely coupled, with the main atmospheric destructive pathway of both species being via reaction with the hydroxyl radical (OH). Currently, most earth system models (ESMs) simulate hydrogen or methane with a prescribed lower boundary condition, which suppresses chemical feedbacks at the surface. In this work, we implement hydrogen emissions and a hydrogen soil uptake scheme into an ESM with free-running methane to demonstrate the capability of a fully interactive hydrogen and methane emissions-driven ESM. We show that the model is able to capture long term trends and seasonal cycles of both species when compared to observations, and find that the inclusion of both fluxes does not impact other chemical species in the model, such as tropospheric ozone. We show that the model can be used under pre-industrial conditions and ~~with a hydrogen pulse experiment~~present day scenarios. The ESM with fully coupled hydrogen and methane chemistry has great potential to be used in future scenarios and to estimate a more accurate global warming potential of hydrogen.

## 1 Introduction

Hydrogen is an alternate energy carrier to fossil fuels (Hydrogen Council, 2020). Transport of hydrogen is prone to leakage, which may result in an increase of its atmospheric abundance. While not a greenhouse gas itself, hydrogen can indirectly contribute to greenhouse gas levels by extending methane lifetime, and increasing stratospheric water vapour and tropospheric ozone (e.g. Warwick et al., 2004, 2023; Tromp et al., 2003; Derwent et al., 2006). The main atmospheric chemical sink for hydrogen is via reaction with the hydroxyl radical (OH), which accounts for ~~$\approx 30\%$~~ $\sim 30\%$ of the atmospheric hydrogen sink (Ehhalt and Rohrer, 2009). Previous studies have found that OH is a competing resource between methane and hydrogen, as methane also reacts with OH as its main sink. Increasing hydrogen concentration therefore causes an extension in methane lifetime ~~,~~ as OH is depleted by reaction with hydrogen (Warwick et al., 2023). Earth system models (ESMs) have typically prescribed methane and hydrogen as fixed lower-boundary ~~concentrations~~ mixing ratios because their sources and sinks are uncertain and their long lifetimes make them sufficiently well-mixed to reproduce global burdens without explicit fluxes (e.g. Sand et al., 2023; Paulot et al., 2021; Warwick et al., 2023; Bryant et al., 2024). This approach also helps prevent model drift that can arise from poorly constrained fluxes. Incorporating surface fluxes, however, enables models to better represent chemistry-climate feedbacks and thus generate more realistic projections of future atmospheric burdens and radiative forcing.

OH is a highly reactive radical, and there is much uncertainty for its reactivity and abundance (Yang et al., 2024; Chen et al., 2024). Given that hydrogen and methane are closely related and impact one another, coupling hydrogen and methane in an ESM will give a better understanding of the role hydrogen plays in the methane feedback factor (Holmes, 2018). This work implements a hydrogen emissions-driven capability with a deposition scheme alongside the methane flux scheme from Folberth et al. (2022) to create a fully interactive hydrogen and methane model. The main sink for atmospheric hydrogen is by soil uptake (~~$\approx 70\%$~~$\sim 70\%$), while the chemical sink via reaction with the OH accounts for (~~$\approx 30\%$~~$\sim 30\%$) (Ehhalt and Rohrer, 2009). We analyse the impacts of an interactive hydrogen scheme on the effects of methane, as well as comparing the simulated hydrogen and methane to observations. We then run the fully interactive ESM under pre-industrial conditions and ~~also with a pulse of hydrogen in a present-day scenario to assess the feedback between these two species.~~ with sustained increased and reduced hydrogen emissions to analyse the methane response to changes in hydrogen under present day scenarios.

## 2 Methods

### 2.1 Model Configuration

The model used in this work is version 1.0 of the UK's Earth System Model (UKESM1.0), using the Unified Model (UM) at version 12.0. The model uses an atmosphere-only configuration (UKESM1.0-AMIP), and is set with 85 vertical levels and on a $1.875° \times 1.25°$ degrees (longitude-latitude) grid. The chemistry scheme implemented in UKESM1.0 is described and evaluated in Archibald et al. (2020). 'Nudged' simulations are set up as described in Telford et al. (2008), and use wind speeds ($u$ and $v$) and air temperature from ERA5 data ~~(https://cds.climate.copernicus.eu/datasets/reanalysis-era5-pressure-levels-monthly-means?tab=overv~~ (https://cds.climate.copernicus.eu/datasets/reanalysis-era5-pressure-levels-monthly-means?tab=overview; Accessed 26/11/25, Hersbach e . The control simulation has been run from 1982 to 2013 with both the hydrogen (time-invariant) and methane (time-varying) configured with a Lower Boundary Condition (LBC) with a uniform spatial distribution. The LBC resets the value of the relevant species at the lowest vertical level after each timestep.

A total of four nudged simulations have been performed to compare the interactive fluxes; a control, two runs with either $H_2$ flux or $CH_4$ flux turned on, and one with both fluxes on. Table 1 shows a full list of the simulations run and a description of each. ~~The Sanderson simulation uses fixed methane LBC with~~ In addition to the four simulations, a fifth simulation using the hydrogen deposition scheme ~~described in Sanderson et al. (2003)~~ from Sanderson et al. (2003) with fixed methane LBC was run (named Sanderson in Table 1) to compare to another deposition scheme. The Sanderson scheme was only run for one year as there is only very limited interannual variability in the forcing soil temperature and soil moisture data from the land surface model, JULES (Pinnington et al., 2018). In addition to the nudged simulations, ~~three~~ four timeslices were also performed. A

**Table 1.** List of simulations. Present day and pre-industrial simulations have been spun up for 30 years. LBC = Lower Boundary Condition, Flux = interactive tracer with emissions and uptake~~.~~, PD = Present day, PI = Pre-industrial, TS = Time Slice, TR = Transient

| Name | Abbreviation | Description |
|---|---|---|
| $H_2$ LBC~~;~~, $CH_4$ LBC Transient | Control | ~~Nudged from 1982.~~ LBC for both $H_2$ and $CH_4$. Nudged from 1982 – 2013 |
| $H_2$ Flux~~;~~, $CH_4$ LBC Transient | ~~H~~TR-$H_2$-flux | Nudged from 1982 – 2013 with $H_2$ emissions |
| $H_2$ LBC~~;~~, $CH_4$ Flux Transient | ~~CH~~TR-$CH_4$-flux | Nudged from 1982 – 2013 with $CH_4$ biogenic, biomass burning and anthropogenic emissions + $CH_4$ flux adjustment (Folberth et al., 2022) |
| $H_2$ Flux~~;~~, $CH_4$ Flux Transient | ~~H~~TR-$H_2$~~;~~ $CH_4$-flux | Nudged from ~~1982 – 2013 with both~~ 1982-2013 with $H_2$ ~~and all~~ emissions and $CH_4$ ~~emissions~~ biogenic, biomass burning and anthropogenic emissions + $CH_4$ flux adjustment |
| $H_2$ Flux~~;~~, $CH_4$ LBC Transient | Sanderson | Nudged with Sanderson hydrogen deposition scheme from 1982 – 1983 with $H_2$ emissions |
| $H_2$ Flux~~;~~, $CH_4$ Flux PD Timeslice | ~~H~~TS-$H_2$~~;~~ $CH_4$-PD | 2020 Present day timeslice. SSP370 $H_2$ emissions for 2020. $CH_4$ emissions are same as Folberth et al. (2022) |
| $H_2$ Flux~~;~~, $CH_4$ Flux ~~Pulse~~ PI Timeslice | TS-$H_2CH_4$-PI | Pre-industrial timeslice from 1850. $H_2$ ~~;~~ and $CH_4$ ~~-Pulse~~ emissions with PI $CH_4$ flux adjustment |
| $H_2$ Flux, $CH_4$ Flux PD ×0.25 $H_2$ emissions | TS-$H_2CH_4$-0.25 | 2020 Present day timeslice with ~~hydrogen pulse. Same emissions as PD timeslice~~ reduced ($\times\frac{1}{4}$) $H_2$ emissions |
| $H_2$ Flux~~;~~, $CH_4$ Flux ~~PI Timeslice~~ PD ×4 $H_2$ ~~;~~ emissions | TS-$H_2$$CH_4$~~-PI~~ -4 | ~~Pre-industrial timeslice from 1850.~~ 2020 Present day timeslice with increased (×4) $H_2$ ~~and $CH_4$ emissions with PI $CH_4$ flux adjustment~~ emissions |

timeslice experiment involves running the model with fixed sea surface temperatures, sea ice, and all other boundary conditions for a given year. One is under pre-industrial (PI) conditions (year 1850), while the other ~~two are~~ is present day conditions (year 2020). ~~One of the present day simulations acts as a control, while the other is a hydrogen pulse experiment.~~ Timeslices for present day (~~H~~TS-$H_2$~~;~~ $CH_4$-PD) and pre-industrial (~~H~~TS-$H_2$~~;~~ $CH_4$-PI) with both interactive hydrogen and $CH_4$ are spun up for 30 years, with the former using $CH_4$ and $H_2$ (derived from CO) emissions from the Coupled Model Intercomparison Phase 6 project, using the Shared Socioeconomic Pathway 3 with a radiative forcing of 7.0 $Wm^{-2}$ at the end of the 21st century i.e., SSP3-7.0 (Rao et al., 2017; Riahi et al., 2017) (see Section 2.2 for the calculation of $H_2$ emissions). Data are analysed over a

5-year period after the initial 25 year spin up, to allow for methane to reach a suitable steady state after 2.5 methane lifetimes. ~~The~~

While the LBC and interactive simulations offer a step by step response with and without interactive $H_2$ ~~;~~ and $CH_4$ ~~Pulse experiment was conducted by setting the initial hydrogen concentration at all levels (vertical and spatial) for the first timestep to 25% higher than the global-averaged surface concentration in the~~ in a nudged scenario, these simulations are not directly comparable due to the differences in treatment of $CH_4$ and $H_2$ ~~;~~ at the surface. In order to make an equal comparison, two additional timeslice simulations were run over the year 2020. The TS-$H_2CH_4$-PD ~~simulation (from 530 ppbv to 662.5 ppbv).~~ run is used as a control, while in the other two simulations all $H_2$ emissions are continuously multiplied by 1/4 (TS-$H_2CH_4$-0.25) and 4 (TS-$H_2CH_4$-4). These simulations are run for ten years to assess the response of $CH_4$ to different levels of $H_2$. The same starting conditions ~~as the H~~are used as the TS-$H_2$~~;~~$CH_4$-PD simulation after the spin up period. Table 1 summarises these simulations.

### 2.2 Hydrogen Emissions

For the sources and quantities of primary hydrogen input to the model, we follow the method of Paulot et al. (2021). Hydrogen is released into the atmosphere from biomass burning and anthropogenic fossil fuel combustion. In addition, natural hydrogen sources associated with marine and terrestrial nitrogen fixation are also included. A summary of the emissions used for the nudged simulations is shown in Figure A2.

As in Paulot et al. (2021), we use carbon monoxide (CO) emissions as a proxy for the evolution of hydrogen emissions trend. To obtain the amount of hydrogen emitted at any given time, we scale the corresponding CO emissions using a source specific ratio. The ratio of CO:$H_2$ for ~~each category (anthropogenic , biomass burning , oceanic and terrestrial)~~ anthropogenic and biomass burning is derived from the period 1995 – 2014, where we have a known estimate of hydrogen emission (Table 1; Paulot et al., 2021) and can calculate the average CO emission over that time from emissions data.

The CO emissions used for the historical proxy are those created for UKESM1.0 for CMIP6 and detailed in Sellar et al. (2020). For anthropogenic and biomass burning emissions we use a historical timeseries (1850 – 2014). Anthropogenic emissions are taken from the Community Emissions Data System (CEDS-2017-05-18; Hoesly et al., 2018). For biomass burning we use those recommended for CMIP6 emissions (van Marle et al., 2017).

A seasonally varying climatology is used for natural emissions. Oceanic emissions use a monthly varying annual cycle for the year 1990 from the POET (Granier et al., 2005) inventory and apply it repeatedly. Terrestrial biosphere emissions are taken from the MACCity-MEGAN emissions inventory (Sindelarova et al., 2014), and a monthly varying annual cycle is taken from a mean of the years 2001 – 2010. All $H_2$ emissions are regridded from their native horizontal resolution to the N96 model grid ($1.875° \times 1.25°$ longitude–latitude, approximately 135 km resolution) conserving mass. The resultant hydrogen emission for ~~each source (anthropogenic , biomass burning , oceanic, and terrestrial) follows~~ anthropogenic and biomass burning sources follow the spatial pattern of the equivalent CO source, but with values rescaled to give the global emission total appropriate for hydrogen. Scalings for oceanic and terrestrial $H_2$ emissions were set as 6 and 3 Tg respectively with the spatial distribution following that of CO as in Paulot et al. (2021). The hydrogen emissions are in agreement with Paulot et al. (2021) as shown in Figure A2.

The year-2020 anthropogenic and biomass burning hydrogen emissions use the same source specific ratios of CO:$H_2$ as described above, and have been applied to year-2020 CO emissions from CMIP6 SSP3-7.0 (Gidden et al., 2019). The total biomass burning and anthropogenic $H_2$ emissions accounted for 7.6 Tg yr$^{-1}$ and 14.9 Tg yr$^{-1}$ respectively. The TS-$H_2CH_4$-PI simulation used the same biomass burning hydrogen emissions as calculated for the nudged simulations, which extend back to 1850 and contributed 13.1 Tg yr$^{-1}$. The monthly varying climatologies for natural oceanic and terrestrial biosphere hydrogen emissions are invariant in time and, thus, are as described above.

## 2.3 $CH_4$ Flux Adjustment

Methane emissions used in the ~~CH4~~ $CH_4$ flux experiments include biomass burning, anthropogenic, and biogenic emissions (Figure A1). Biogenic wetland emissions and soil uptake are calculated interactively within the model, whereas all other emissions are prescribed (Hoesly et al., 2018; Fung et al., 1991). To reconcile simulated global mean surface methane concentrations with observations, a residual methane surface exchange flux, or flux adjustment, is applied in all simulations, following FFolberth et al. (2022). This flux represents the net ~~“missing”~~ “missing” sources or sinks required in the emissions-driven configuration of UKESM to capture global methane observations. Separate flux adjustments are used for the pre-industrial (~~H~~TS-$H_2$~~;~~$CH_4$-PI) and present-day (~~H~~TS-$H_2$~~;~~$CH_4$-PD) timeslice simulations, as well as for the nudged simulations (~~CH4-flux and H2; CH4-flux~~TR-$CH_4$-flux and TR-$H_2CH_4$-flux). The PI and PD adjustments are taken directly from Folberth et al. (2022), with magnitudes of 5 Tg yr$^{-1}$ ~~for the PI~~ and 48 Tg yr$^{-1}$ ~~for the PD period~~respectively. In the nudged simulations, a larger adjustment is required than in the PD timeslice because interactive wetland emissions are lower (135 Tg yr$^{-1}$ versus 190 Tg yr$^{-1}$ in the PD simulation). This reduction in wetland emissions is consistent with a smaller global wetland fraction in the nudged configuration (0.0321) compared with the PD timeslice simulation (0.0358, an 11% increase). To compensate for the reduced wetland source, the flux adjustment from the PD simulation was scaled by 3.5 in the nudged simulations ~~which~~ to enable the model to capture the growth in surface global mean methane during the 1980s. Note that the flux adjustment is static across all years. ~~.~~

## 2.4 $H_2$ Soil Deposition Scheme

The model uses a two-layer hydrogen soil uptake scheme to calculate soil resistance (rc) based on the work by Ehhalt and Rohrer (2013) and Paulot et al. (2021), and used in Brown et al. (2025). ~~Processes in the first layer include~~ The first layer represents the diffusion of hydrogen through the top layer of soil, while the second layer represents the loss from the microbial uptake of hydrogen. Two soil types, sand and loam, are included in the diffusion and microbial uptake parameterisation. The sand fraction of each gridbox is used to classify the soil type, with the remaining fractions (loam and clay) classified as loam. This is likely to lead to a slight overestimate in soil uptake in areas of high clay content, as hydrogen uptake in clays is known to be lower than loam (Bertagni et al., 2021; Cowan et al., 2024). The scheme ~~already~~ also has a tuning parameter, $\alpha$, which was

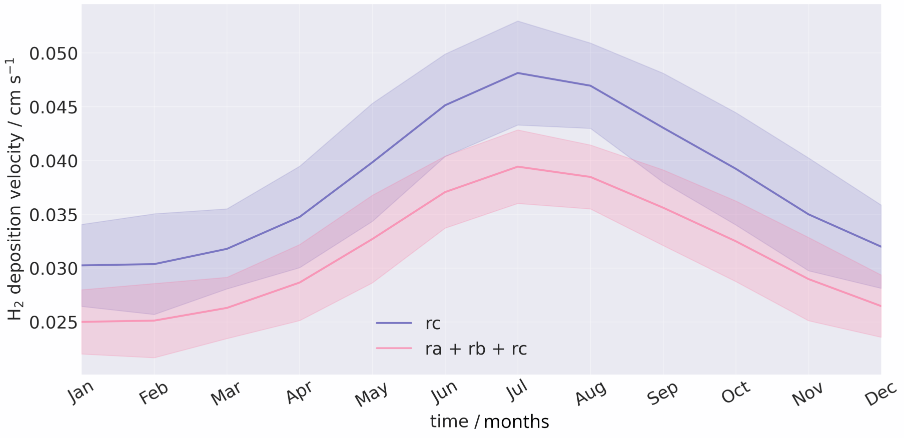

**Figure 1.** Monthly, land averaged hydrogen deposition velocity for simulation ~~H~~TR-$H_2$-flux ($H_2$ Flux; $CH_4$ LBC) between 1982-2013 with all resistances (pink) and with only hydrogen deposition velocity (purple). Shaded areas indicate two standard deviations.

scaled to the tropospheric hydrogen global burden to approximately $155\,\text{Tg}$ to be ~~with~~ in line results from Ehhalt and Rohrer (2009). Full details of the deposition scheme are given in Section A1.

~~Further to the soil resistance (rc), the model also includes~~ Different hydrogen deposition schemes vary in the inclusion of other deposition resistances (e.g. Bertagni et al., 2021). In this model, aerodynamic (ra) and laminar (rb) resistances are incorporated (Marrero and Mason, 1972; Hicks et al., 1987). Including these resistances results in the global hydrogen uptake to decrease by $0.007\,\text{cm s}^{-1}$ (average $17.6\%$ decrease). The averaged land deposition velocity with all resistances is $0.0314\,\text{cm s}^{-1}$, while with just the uptake resistance the deposition velocity is $0.0380\,\text{cm s}^{-1}$. Figure 1 shows the monthly, land-averaged hydrogen deposition velocity with (pink) and without (purple) the additional resistances averaged between 1982-2013. The largest changes due to aerodynamic and laminar resistances occur over South America and Africa (excluding the desert), where deposition velocities can have a temporally averaged maximum difference up to $0.14\,\text{cm s}^{-1}$.

An offline version of this model used in Brown et al. (2025) implemented a lower limit for uptake occurring in deserts, and a soil moisture cap for areas with a high soil moisture content (SMC). Both of these features are used in this model. If the volumetric SMC falls below ~~the~~ a set of thresholds, the values for $f_s(\Theta_a)$ or $f_l(\Theta_a)$, which govern the microbial uptake, are set to one third of the minimum values under those temperature and soil porosity conditions, reflective of the findings in Jordaan et al. (2020) (see Appendix A, Equations A9 and A12 for more detail). For desert environments where the volumetric SMC is often below the threshold, this prevents the hydrogen deposition from immediately being set to zero, and allowing for uptake to occur in desert environments.

At locations of high volumetric SMC relative to the soil porosity, hydrogen cannot diffuse through the top layer of soil and hydrogen deposition is very low. In UKESM1.0, the ratio of volumetric SMC to total porosity ($\frac{\text{volumetric SMC}}{\text{soil porosity}}$) is very high at northern latitudes with an annual average of $> 0.85$. Observed volumetric SMC during summer in these regions is between $0.15 - 0.3\,\text{m}^3\ \text{m}^{-3}$ (Dorigo et al., 2023), which, if using the soil porosity from UKESM1.0, produces $\frac{\text{volumetric SMC}}{\text{soil porosity}} \leq 60\%$.

This high ratio from UKESM1.0 is likely to be inaccurate due to the soil porosity not capturing the large coverage of peatland at these latitudes. Soil porosity is calculated using sand fraction and does not take into account soils such as peatlands, which have been found to have a high hydrogen uptake (Simmonds et al., 2011). In order to compensate for the high volumetric SMC to porosity ratio, the $\frac{\text{volumetric SMC}}{\text{soil porosity}}$ ratio in the hydrogen deposition scheme is capped at $70\%$. The volumetric SMC is adjusted so the maximum ratio does not exceed this value.

## 3 Evaluation of $H_2$ Deposition

The hydrogen deposition previously implemented in UKESM1.0 used the scheme from Sanderson et al. (2003). This deposition uptake was based on soil land type and scaled the deposition linearly or quadratically with soil moisture depending on the land type. While this produces global deposition velocities in line with other global hydrogen deposition values (see Sand et al., 2023), it does not include uptake in deserts, and is limited by requiring the land-use type within a grid cell. The scheme adapted from Paulot et al. (2021), which is used in this work allows for an interactive hydrogen flux, is dependent on soil properties and thus can be used for scenarios in which the land type is not known or prescribed (e.g. pre-industrial conditions, future climate simulations).

Figure 2 shows the comparison of hydrogen deposition velocities between the scheme adapted from Paulot et al. (2021) and the scheme from Sanderson et al. (2003). Both simulations have the same model configuration, using the same hydrogen emissions, ‘nudged’ winds and air temperature from ERA5 data as per Telford et al. (2008). The ~~H~~TR-$H_2$-flux simulation has a greater hydrogen deposition in the northern hemisphere ($> 30°$ N) than in the Sanderson scheme, with deposition increase of $0.02-0.04\,\mathrm{cm\,s^{-1}}$ in North America and Central Asia (Figure 2c). This is also seen by the dash-dotted lines in Figure 2d, which show the land-average deposition above 30° N; the ~~H~~TR-$H_2$-flux simulation (purple) is between $0.002-0.005\,\mathrm{cm\,s^{-1}}$ greater than the Sanderson et al. (2003) (pink) simulation. Both simulations share a seasonal cycle which is dominant in northern latitudes, with the Sanderson et al. (2003) simulation having a larger amplitude in seasonality. The ~~H~~TR-$H_2$-flux simulation has an overall higher deposition velocity (9.2% higher) throughout the year than that of the Sanderson et al. (2003) scheme (thick solid lines in Figure 2d), with an annual, land-averaged mean of $0.0312\,\mathrm{cm\,s^{-1}}$ compared to $0.0285\,\mathrm{cm\,s^{-1}}$ respectively. This is due to uptake occurring in the desert, as well as in the tropics and at high northern latitudes.

Figure 3 shows simulated hydrogen deposition against observations at four different sites, all of which are located in the northern hemisphere. The land types of a) Harvard and d) Loppi are deciduous and boreal forests respectively, while b) Gif-sur-Yvette and c) Mace Head are grassland/agriculture and peatbogs respectively. The soil types of all sites are different, with Harvard Forest as sandy loam, Loppi as mineral and peat soils, and Mace Head as peatland (Gif-sur-Yvette not given). ~~H~~TR-$H_2$-flux and ~~H~~TR-$H_2$~~; ~~$CH_4$-flux simulations were compared against the observations. Both simulations produce very similar hydrogen velocities, globally and at all individual sites, which is expected as there is little atmospheric influence on the hydrogen deposition velocities. Shaded areas show the range of deposition velocities from ~~CMIP ~~CMIP6 model inputs calculated in Brown et al. (2025), while the purple line shows the deposition velocities from the Sanderson simulation~~, averaged~~

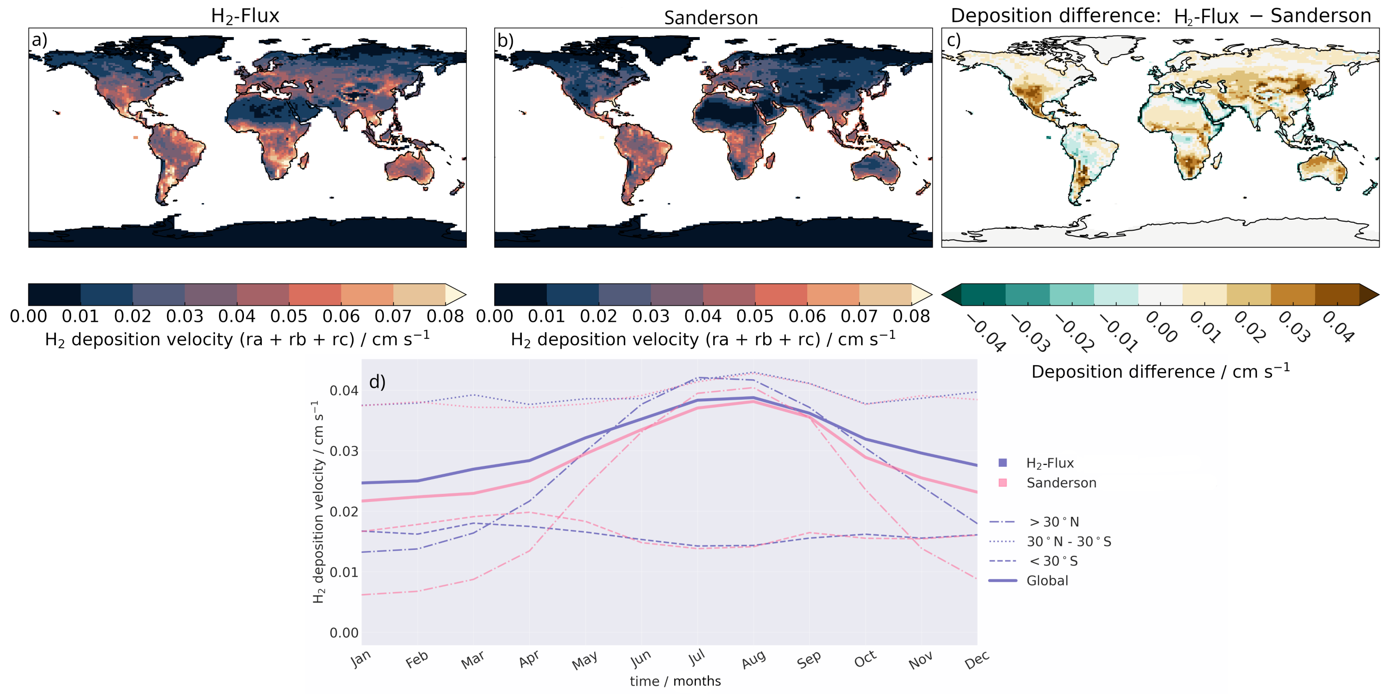

**Figure 2.** Annually averaged hydrogen deposition velocity in 1982 for a) ~~H~~TR-$H_2$-flux using deposition scheme adapted from Paulot et al. (2021), b) Sanderson et al. (2003) deposition ($H_2$ Flux; $CH_4$ LBC), and c) difference between the two schemes (a – b). d) Land-averaged monthly mean hydrogen deposition velocities of (purple) ~~H~~TR-$H_2$-flux and (pink) Sanderson for 1982. Linestyles indicate 30° latitude bands into which data have been divided, with the thickest line showing the global-averaged deposition.

~~over one year~~. Compared to observations and other simulations, the ~~H~~TR-$H_2$-flux and ~~H~~TR-$H_2$~~;~~ $CH_4$-flux simulations tend to overestimate deposition velocity, with the exception of Mace Head.

At Mace Head, the hydrogen deposition velocities are underpredicted in April-May and are outside of the range of observed deposition velocities, although within the standard deviation of observations for the remaining months (June to October). Gif-sur-Yvette lacks observations during the summer months and thus there is no defined peak to which the simulations can be compared directly. However, between November-April, deposition velocities are within $0.005\,\mathrm{cm\ s^{-1}}$ of the observations. In both Harvard Forest a) and Loppi b), deposition is overpredicted by $0.02 - 0.04\,\mathrm{cm\ s^{-1}}$, with the largest discrepancy for both sites occurring in the summer months. The CMIP6 range also overpredicts deposition at these sites, although not to the same extent (up to $0.02\,\mathrm{cm\ s^{-1}}$). Overestimates in the ~~H~~TR-$H_2$-flux and ~~H~~TR-$H_2$~~;~~ $CH_4$-flux deposition velocities correspond with underestimates in hydrogen ~~concentrations~~ mixing ratios in the northern hemisphere. ~~This is further discussed in in Section 4.1.~~

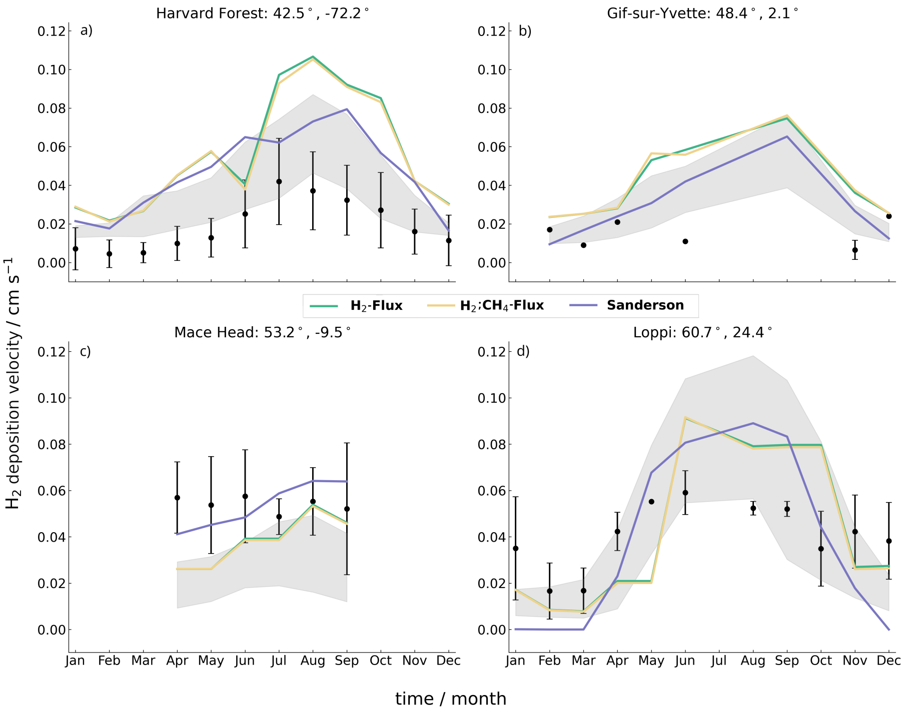

**Figure 3.** ~~Observed~~ Monthly mean observed hydrogen deposition velocities averaged across years where possible (points) compared with (green) ~~H~~TR-H$_2$-flux, (yellow) ~~H~~TR-H$_2$~~;~~ CH$_4$-flux, and (purple) Sanderson simulated velocities for a) Harvard Forest (2010 – 2012; Meredith et al., 2017), b) Gif-sur-Yvette (2011; Belviso et al., 2013), c) Mace Head (1995 – 2008; Simmonds et al., 2011), and d) Loppi (2004 – 2006; Lallo et al., 2008). Error bars show one standard deviation across years. Shaded areas show the range of deposition velocities from ~~CMIP~~ CMIP6 model inputs calculated in Brown et al. (2025).

## 4 Results

### 4.1 Comparison to Atmospheric Observations

In order to evaluate the skill of the model, the hydrogen and methane outputs are first compared to multiple years of observations (Prinn et al., 2018). Figure 4 compares surface observations of a) hydrogen and b) methane with the simulated ~~H~~TR-H$_2$~~;~~ CH$_4$-flux values. Observations at two stations are shown; Mace Head in the northern hemisphere (MHD; green) and Cape Grim in the southern hemisphere (CGO; orange). The latitude and longitude of simulated values were matched by nearest neighbour to the closest location of the station sites. The simulated hydrogen ~~concentrations~~ mixing ratios for Mace Head are in good agreement with the observations. There is a small overprediction up to 15 ppbv between 1994 – 2000, but after the year 2000 the simulated hydrogen is in line with the observations. These sites were chosen as they had the longest continuous H$_2$ record available in the northern and southern Hemispheres, as well as their locations' suitability for monitoring baseline atmospheric conditions. The simulated hydrogen captures the trend post 2003 at Cape Grim, but does not do as well prior to this. Furthermore at Cape

Grim, hydrogen is consistently overpredicted during the southern summer, where hydrogen can be up to 35 ppbv greater than observed values. The minimum hydrogen ~~concentrations~~ mixing ratios are captured during southern winter, suggesting that the seasonal cycle of hydrogen is too strong in the model. This may be due to too extreme changes in soil moisture between the winter and summer months (Pinnington et al., 2018).

Simulated methane is slightly underpredicted when compared with observations from Cape Grim. This is seen in Figure 4b from 1995 onwards, where there is a 50 ppbv low bias with respect to observations in the model. Similarly, in the northern hemisphere, methane at Mace Head is generally in good agreement with observations from 1997 onwards (50 ppbv excess). Between $1992-1997$, there is a larger difference, which reaches up to 100 ppbv. The model captures the overall trend and seasonal cycle of observations.

Further to these two sites, the simulated hydrogen is compared to observations at all NOAA stations (Pétron et al., 2024). Observed data have been monthly averaged to match the same time resolution as the modelled data. Simulated hydrogen has been matched to observations by nearest latitude and longitude, and time up to the year ~~2014.~~ 2013. Hydrogen observations after the year 2013 are discarded as simulations were run for the historical time period used in CMIP6, where there was availability of historical emissions. Figure 5a summarises the variance via normalised standard deviation (NSD) and correlation between simulated and observed hydrogen, while Figure 5b shows the average surface hydrogen ~~concentration for the H~~mixing ratios for the TR-$H_2$~~;~~ $CH_4$-flux simulation (on map) and observation sites (points).

In Figure 5a, sites in the northern hemisphere are blue, while southern sites are in red. Table A1 gives the numerical key for each site. Values close to the point marked ‘REF’ (which is 1) show that the standard deviation of the model and observation site are very similar, implying they have a similar variation. The correlation conducted uses a standard Pearson’s correlation test, and only stations with more than 20 datapoints pre-2014 were used in the experiment. Values with a higher correlation indicate that the seasonal trend of observed hydrogen is captured.

In Figure 5a, a greater proportion of southern sites (dark red) have a high correlation ($> 0.8$), suggesting they capture the seasonal trend. The NSD tends to be greater than 1, implying that there is too much variation in the modelled data and that, while the seasonal cycle is captured well, the amplitude in the simulated data is larger than the observations. For northern sites, there is a spread of how well the simulated hydrogen captures the variation from observations. At sites where the model has too much variation (NSD $> 1$), the correlation tends to be greater (between $0.65-0.95$), similar to the southern sites. This is similar to the findings from the deposition comparison at Harvard Forest and Loppi (Figures 3a and 3b), where there is too much deposition occurring during the summer.

Values with an NSD $< 1$ tend to have a lower correlation, suggesting the model does not capture the observed variation at these sites. Overall, most sites have an NSD around 1 and a correlation between $0.6-0.9$, indicating the simulation captures the seasonal spread and cycle.

Figure 5b shows the simulated surface hydrogen ~~concentration~~ mixing ratio averaged from $2008-2013$ with the averaged hydrogen ~~concentration~~ mixing ratio from all sites given as points. The hydrogen mixing ratio is high ($> 580$ ppbv) in Africa between 5°N-25°S due to biomass burning and natural emissions, despite the larger deposition velocity over that region. The simulated data captures the hydrogen mixing ratios within 20 ppbv at nearly all observation sites. The exception to this is the

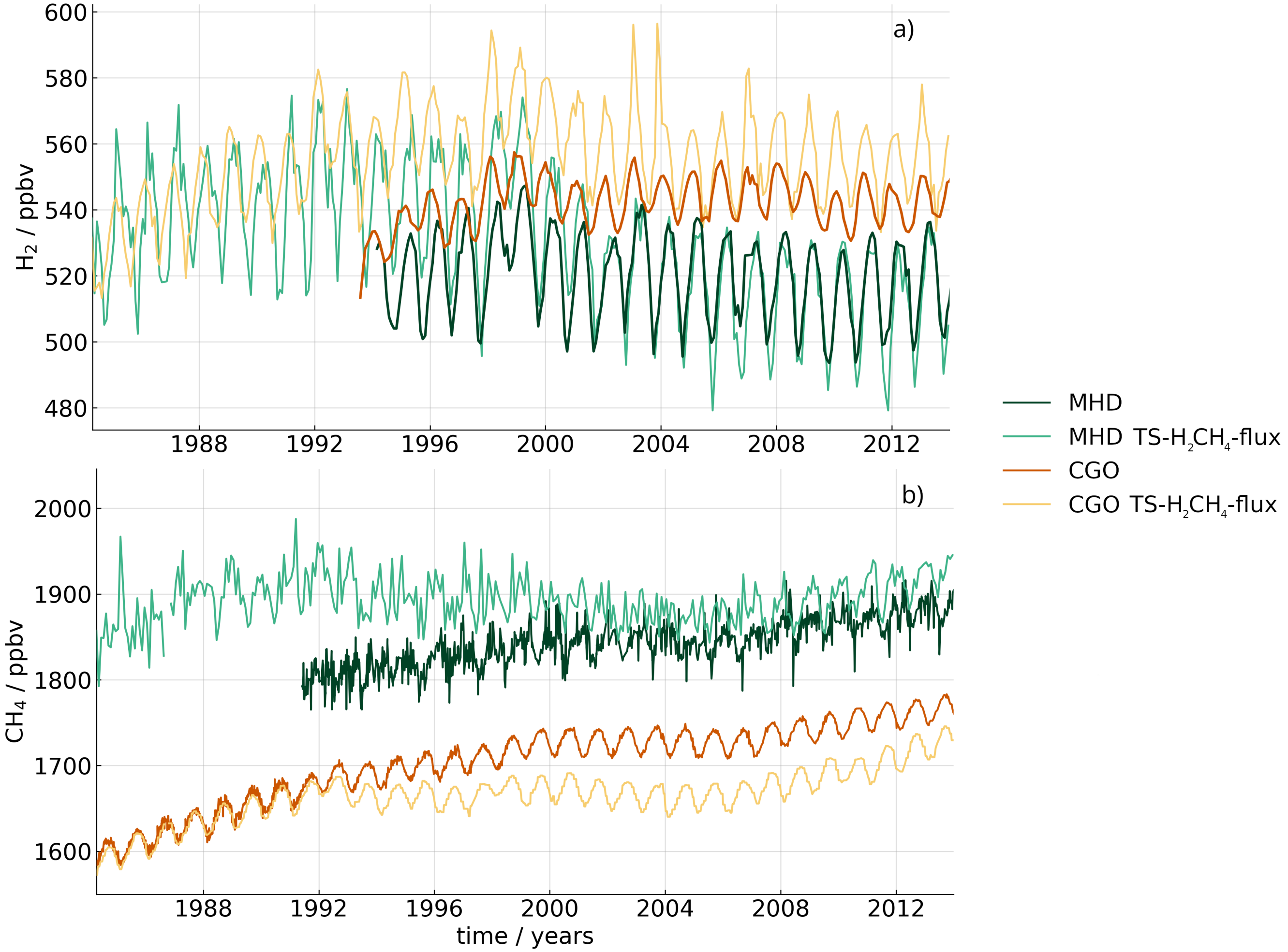

**Figure 4.** Time series of Mace Head for (MHD: dark green) observations and (light green) ~~H~~TR-H$_2$~~;~~ CH$_4$-flux simulation, and Cape Grim (CGO: orange) observations and (yellow) ~~H~~TR-H$_2$~~;~~ CH$_4$-flux for a) hydrogen (observations: 1994-2013) and b) methane (observations: 1985-2013).

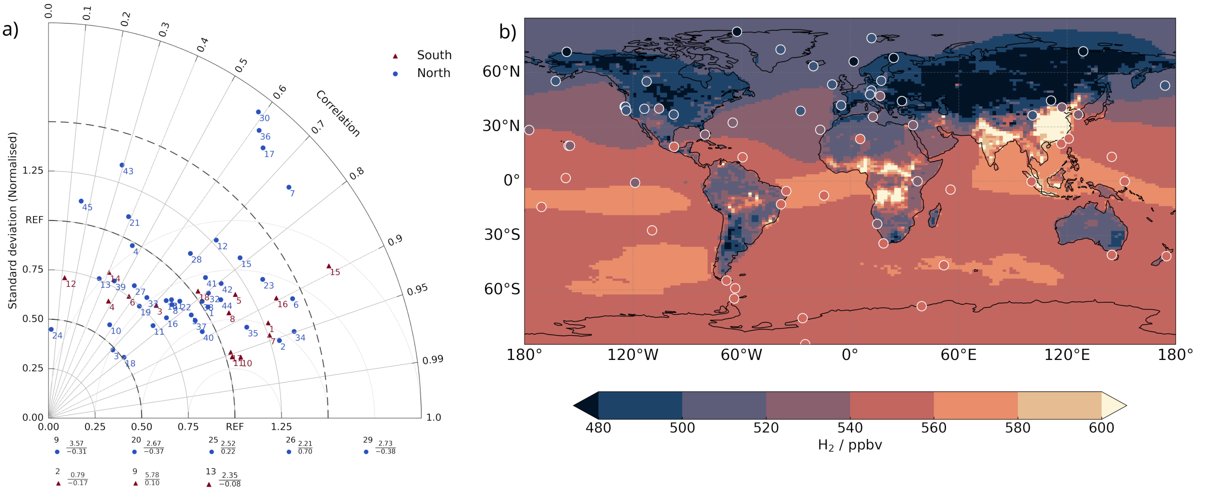

**Figure 5.** a) Taylor diagram showing Pearson's correlation and the standard deviation of modelled data (~~H~~TR-$H_2$~~;~~ $CH_4$-flux) normalised to observations for all different sites. Red triangles show sites in the southern hemisphere, while blue triangles show sites in the northern hemisphere. Anomalies with either too high a NSD or negative correlation are excluded from the diagram and written below with the format $\frac{\text{normalised standard deviation}}{\text{correlation}}$. Labels correspond to sites as given in Table A1. b) Map of averaged surface hydrogen ~~concentration~~ mixing ratio from ~~H~~TR-$H_2$~~;~~ $CH_4$-flux run overlaid with averaged hydrogen ~~concentrations~~ mixing ratios from each NOAA site. All simulated data are averaged between 2008 − 2013.

very high ($>$ 620 ppbv) hydrogen ~~concentration~~ mixing ratio over China and India, which results from the combination of anthropogenic emissions and orography in the model which is known to lead to an overestimation in emissions (Hayman et al., 2014). Overall, the model slightly overpredicts hydrogen in the southern hemisphere by an average of 13.2 ppbv, while in the northern hemisphere there is a small averaged underprediction of 2.1 ppbv. ~~This is likely because the soil sink is too strong during the northern summer months and too much hydrogen is being deposited, as implied by Figures 3a and 3b.~~ In general, the model is able to capture the average magnitude of hydrogen ~~concentration~~ mixing ratios at most sites, and replicates similar correlations and variations to those in the observations.

### 4.2 ~~Effect~~ Impact of Fluxes on Atmospheric Composition

Ozone and OH are both trace gases sensitive to chemical fluctuations in the atmosphere, due to their high reactivity. Global methane ~~concentrations~~ mixing ratios are relatively unchanged with interactive $CH_4$, and there is a small increase in the global hydrogen ~~concentration~~ mixing ratio (from 500 ppbv in the control to 550 ppbv in the ~~H~~TR-$H_2$-flux simulation for 2008 − 2013) when adding in interactive $H_2$ (Warwick et al., 2023). Thus, as expected when adding in both the hydrogen and methane flux, there is minimal impact on tropospheric ozone or OH, as shown in Figure 6. There is up to a 40 ppbv change in ozone between the control and TR-$H_2CH_4$-flux simulation, which corresponds to a 4% decrease. Similarly, there is less than $5 \times 10^4$ molecules

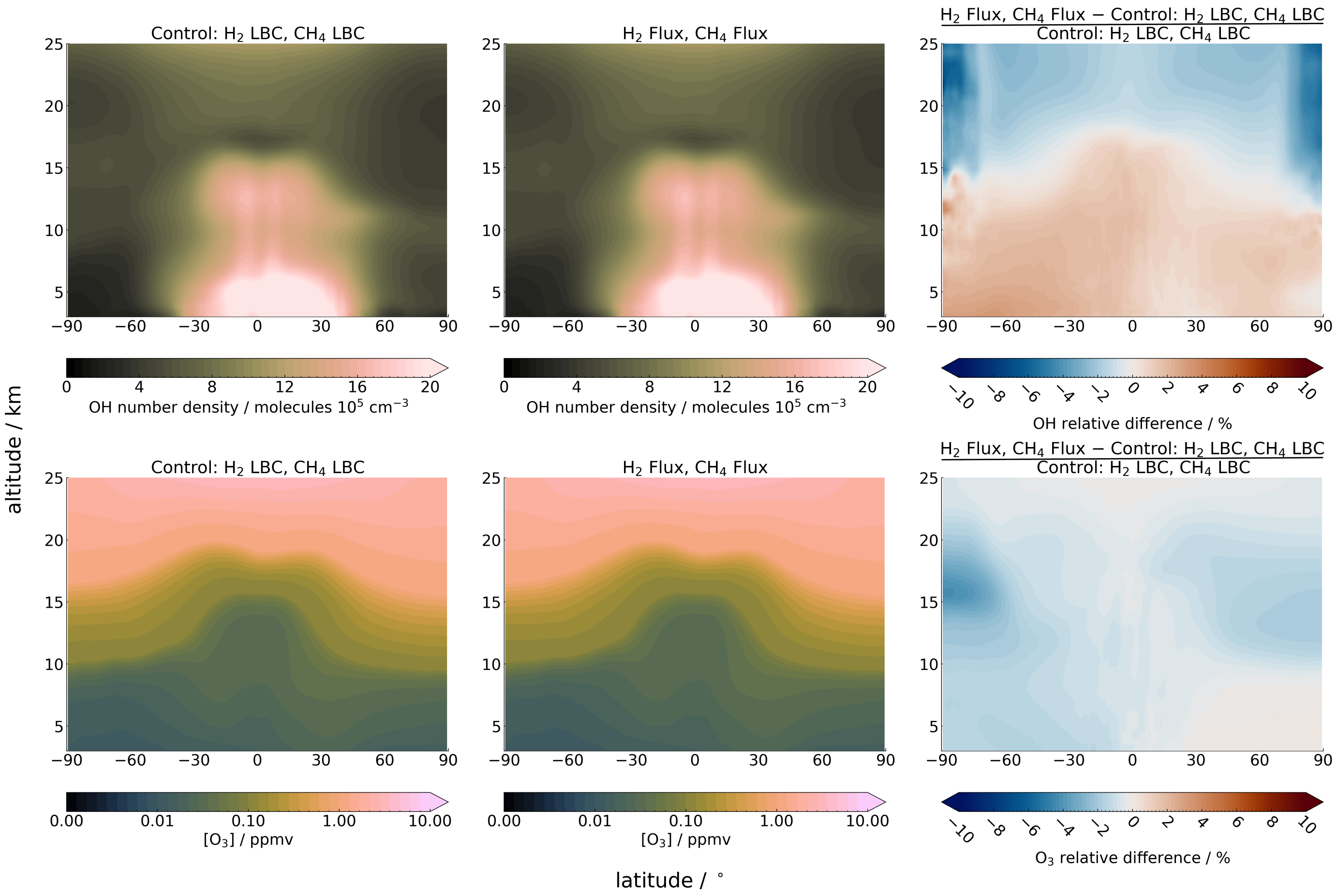

**Figure 6.** Zonally averaged (top) OH concentration and (bottom) ozone ~~concentration~~ mixing ratio for the (left) control simulation, (middle) ~~H~~TR-$H_2$~~;~~ $CH_4$-flux simulation, and (right) the relative difference between the two ((~~Control — H~~TR-$H_2$~~;~~ $CH_4$-flux − Control)/Control) averaged between 2008 – 2013. Red (blue) shows an increase (decrease) from the control.~~Note the non-linearity of scales.~~

cm$^{-3}$ increase in OH density in the troposphere (3% increase), and a decrease of $4 \times 10^4$ molecules cm$^{-3}$ in the stratosphere (5% decrease).

There is a $30-60$ ppbv change in ozone between the control and ~~H~~TR-$H_2$~~;~~ $CH_4$-flux simulation in the troposphere ($< 0.02\%$ increase) and stratosphere ($0.06\%$ decrease). Similarly, there is less than $5 \times 10^4$ molecules cm$^{-3}$ increase in OH density at the surface with both hydrogen and methane flux ($< 0.02\%$ change).

The global surface average of hydrogen and methane is shown in Figure 7. In both the ~~H~~TR-$H_2$~~;~~ $CH_4$-flux and ~~H~~TR-$H_2$-flux simulations, global surface hydrogen equilibrates to 545 ppbv with an average ±12 ppbv seasonal cycle. In 1992 and 1998, there are sharp increases of hydrogen due to the increase of biomass burning in these years (Figure A2), and, in 2002, hydrogen equilibrates to between $540-550$ pbbv. The ~~addition of the methane~~ replacement of the fixed methane LBC to flux has little

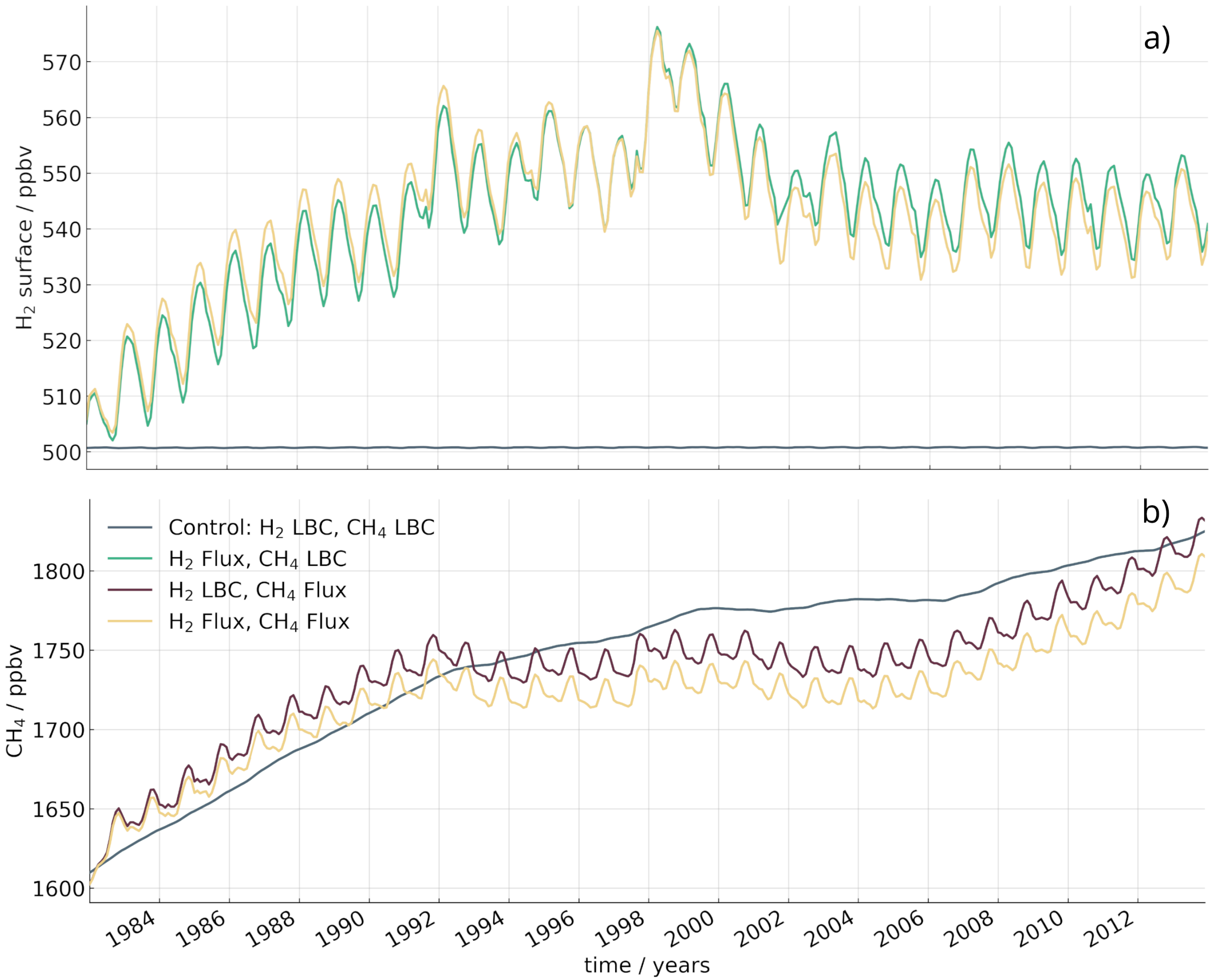

**Figure 7.** a) Globally averaged surface hydrogen from the (grey) control, (green) ~~H~~TR-$H_2$-flux, and (yellow) ~~H~~TR-$H_2$~~;~~ $CH_4$-flux simulations from 1982 to 2013. Both the control and the ~~CH~~TR-$CH_4$-flux simulation have hydrogen set to 500 ppbv at the surface. b) Globally averaged surface methane from the (grey) control, (red) ~~CH~~TR-$CH_4$-flux, and (yellow) ~~H~~TR-$H_2$~~;~~ $CH_4$-flux simulations

impact on hydrogen both globally averaged and across all latitudes (not shown). The control and ~~CH~~TR-$CH_4$-flux simulations both use a fixed $H_2$ LBC of 500 ppbv, which is constant across all times of year and latitude.

Figure 7b shows the surface global methane from the (grey) control and with methane flux with (red) $H_2$ LBC and (yellow) hydrogen flux implemented. Between 1996 − 2012, ~~methane~~ the surface methane mixing ratio in both simulations is slightly below the control by up to 30 ppbv (∼ 1.7% difference). The two simulations with methane flux are in good agreement with the fixed LBC values (the latter of which is based on observations). They capture both the trend pre-1992 and the levelling off of methane abundance between 1998 − 2007, as well as the increasing trend after 2007.

~~Methane~~ The global averaged surface methane mixing ratio decreases when the fixed $H_2$ LBC is replaced by $H_2$ flux; the global, surface average methane is approximately ~~10 ppbv lower~~ 20 ppbv lower from 1998 onwards. The decrease in methane in the ~~H~~TR-$H_2$~~;~~ $CH_4$-flux simulation occurs across all latitudes, with a greater decrease occurring in the northern hemisphere (not shown). ~~One possible explanation could be due to an increase in OH from the increased hydrogen. The main atmospheric sink of methane is reaction via OH and thus dependent on OH availability;~~

$$CH_4 + OH \rightarrow CH_3 + H_2O$$

~~To investigate further, we analyse the main chemical loss reactions (or fluxes) for hydrogen and methane. For methane, the dominant loss is kCH$_4$OHwhere species in brackets are their concentrations and k is the rate constant for the reaction. For hydrogen, the loss terms are k$_1$H$_2$Oand k$_2$~~

One explanation for this is due to the change in surface distribution for $H_2$ mixing ratio which impacts the OH ~~, via the reactions;~~

$$H_2 + O \rightarrow OH + H$$

~~where the O can either be O($^3$P) or O($^1$D), and,~~

$$H_2 + OH \rightarrow H_2O + H$$

~~with the latter being the dominant loss. Figure A3 shows the hydrogen and methane chemical loss; $H_2$ chemical loss increases when $H_2$ flux is implemented into the model, while the $CH_4$ loss via OH decreases~~reactivity. This is ~~expected, given that hydrogen concentration has increased and methane concentration has decreased. The loss rates are dominated by these changes in $H_2$and $CH_4$respectively, and the OH activity cannot be identified.By dividing through by each respective species, these shows the rate coefficients which are not a function of hydrogen and methane concentrations. The end column of~~ a result from the technical differences in simulations (e.g. interactive flux vs fixed LBC). Figure 8 shows the ~~differences~~ one over the rate coefficient of (top) ~~hydrogen lifetime via~~ $H_2$ chemical loss and (bottom) $CH_4$ ~~lifetime via OH loss or~~ loss via OH ($\frac{1}{k[OH]}$ ~~of methane loss~~), which shows the OH reactivity of these reactions, and simultaneously the respective chemical lifetimes of $H_2$ and $CH_4$. Blue (red) indicates ~~an increase (decrease )~~ a decrease (increase) in lifetimes when $H_2$ flux is included, relative to the simulation with fixed $H_2$ LBC.

~~Zonally averaged (top) $H_2$ chemical loss lifetime and (bottom) $CH_4$ lifetime via OH for (left) $CH_4$-flux simulation, (middle) $H_2$; $CH_4$-flux simulation, and (right) relative difference between the two ($CH_4$-flux − $H_2$; $CH_4$-flux) averaged between 2008 – 2013. Red (blue) shows an increase (decrease) from the $CH_4$-flux. Note the non-linearity of scales. The stratosphere has been masked out to reduce noise.~~

~~In the northern hemisphere , there is an increase in the chemical loss rate both for~~ The surface hydrogen mixing ratio in the southern hemisphere increases up to 580 ppbv (as seen in Figure 5b), while decreasing in the northern hemisphere down to $< 480$ ppbv. The shift in hydrogen distribution causes a change in OH reactivity. In the southern hemisphere, the $CH_4$ ~~and $H_2$ (redin right column,~~ lifetime via OH increases by up to 0.4%, which can be seen at the surface between 30° − 60° S (red) in bottom right panel Figure 8. In the northern hemisphere, the $CH_4$ lifetime via OH decreases by $\sim 0.3\%$ (blue in top right panel of Figure 8). This ~~implies that the increase~~ is a result of the reduction in $H_2$ ~~loss rate is causing an increase in the~~ mixing ratio at the surface in the northern hemisphere, which is directly due to the stronger soil uptake over northern American and Siberia.

The different surface set ups (fixed LBC versus interactive flux) are not a fair direct comparison of the response of $CH_4$ to $H_2$. To examine the impact of a change in $H_2$ on $CH_4$ without the added complication of the fixed LBCs, three additional timeslice simulations were analysed; a control (TS-$H_2$$CH_4$~~loss rate at these latitudes. The chemical loss of hydrogen is caused by Equations **??** and **??**. The former of these reactions directly produces a OH molecule, while the latter could potentially generate more OH radicals by creating HO~~-PD), one with reduced $H_2$ emissions (25% reduction; TS-$H_2$$CH_4$-0.25), and another with increased $H_2$ emissions (400% increase;

$$\mathrm{H} + \mathrm{O_2} + M \rightarrow \mathrm{HO_2} + M$$

~~and reacting with $NO_X$:~~

$$\mathrm{HO_2} + \mathrm{NO} \rightarrow \mathrm{NO_2} + \mathbf{OH}$$

$$\mathrm{NO_2} + h\nu \rightarrow \mathrm{NO} + \mathrm{O}$$

$$\mathrm{O} + \mathrm{O_2} + M \rightarrow \mathrm{O_3} + M$$

~~Ozone can break down to indirectly produce more OH radicals:~~

$$\mathrm{O_3} + h\nu \rightarrow \mathrm{O(^1D)} + \mathrm{O_2}$$

$$\mathrm{O(^1D)} + \mathrm{H_2O} \rightarrow \mathbf{2OH}$$

~~We find there is an increasein kHO~~TS-$H_2$~~NOat the surface which could support this mechanism, however it is not asymmetric between hemispheres and does not match up directly at the same latitudes (Figure **??**~~$CH_4$-4). Figure 9 summarises the globally

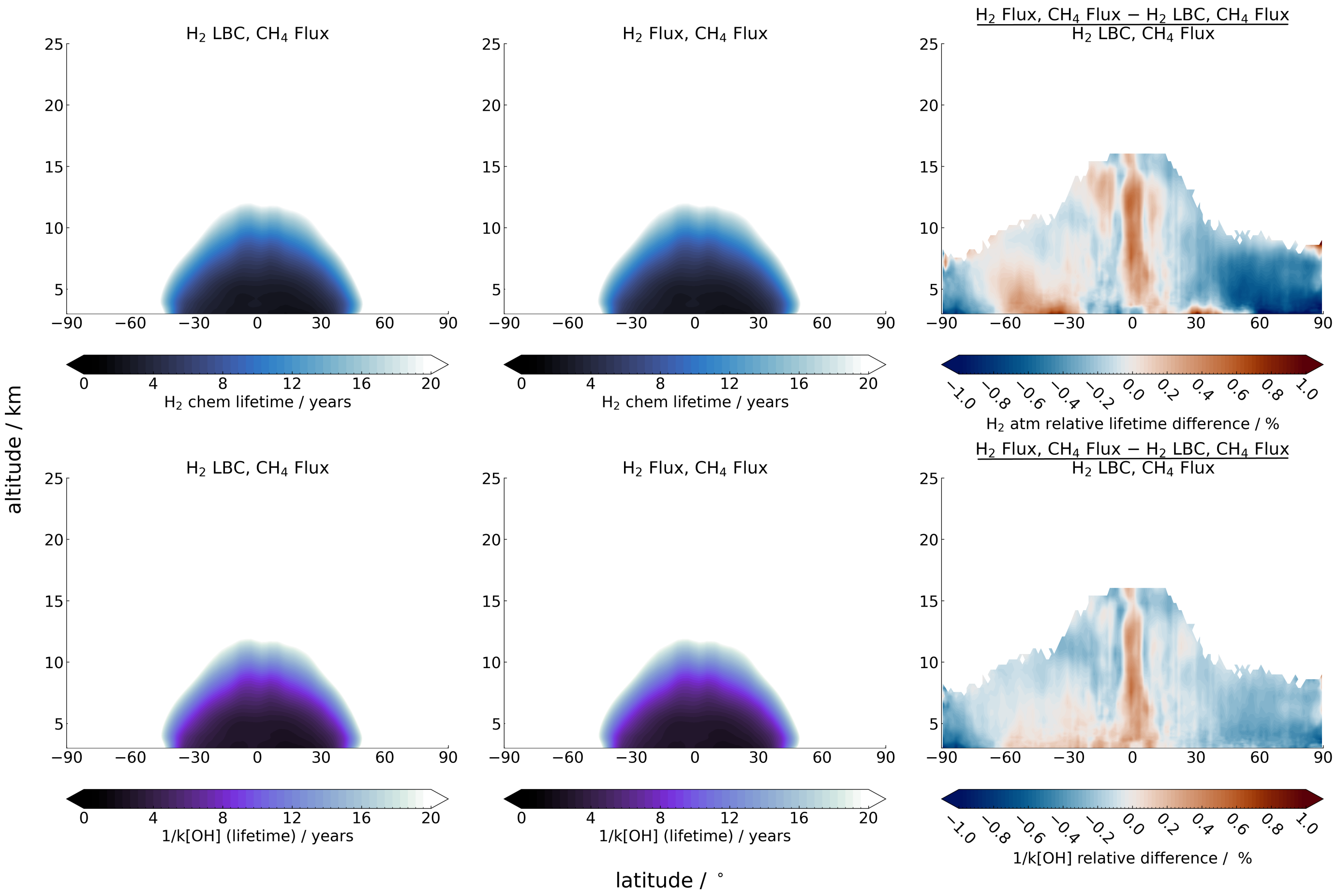

**Figure 8.** Zonally averaged (top) $H_2$ chemical loss lifetime and (bottom) $CH_4$ lifetime via OH for (left) TR-$CH_4$-flux simulation, (middle) TR-$H_2CH_4$-flux simulation, and (right) relative difference between the two ($CH_4$-flux − TR-$H_2CH_4$-flux) averaged between 2008 – 2013. Red (blue) shows an increase (decrease) in lifetimes from the TR-$CH_4$-flux. The stratosphere has been masked out to reduce noise.

averaged surface mixing ratios of (a) $H_2$ and (b) $CH_4$ for 10 years. Figure 9c shows the monthly, globally average surface difference between the control and the altered emissions simulations (control – altered emissions). The black line shows there is no change from the control. The TS-$H_2CH_4$-4 simulation shows that $CH_4$ increases as $H_2$ increases. In particular, there is a non-linear relationship between the two species in the $\times 4$ $H_2$ emission simulation. This is likely due to $H_2$ reaching steady state much quicker than $CH_4$ as its lifetime is shorter (2 years compared to 10 years), while $CH_4$ continues to increase in response to $H_2$ (Figure 9c).

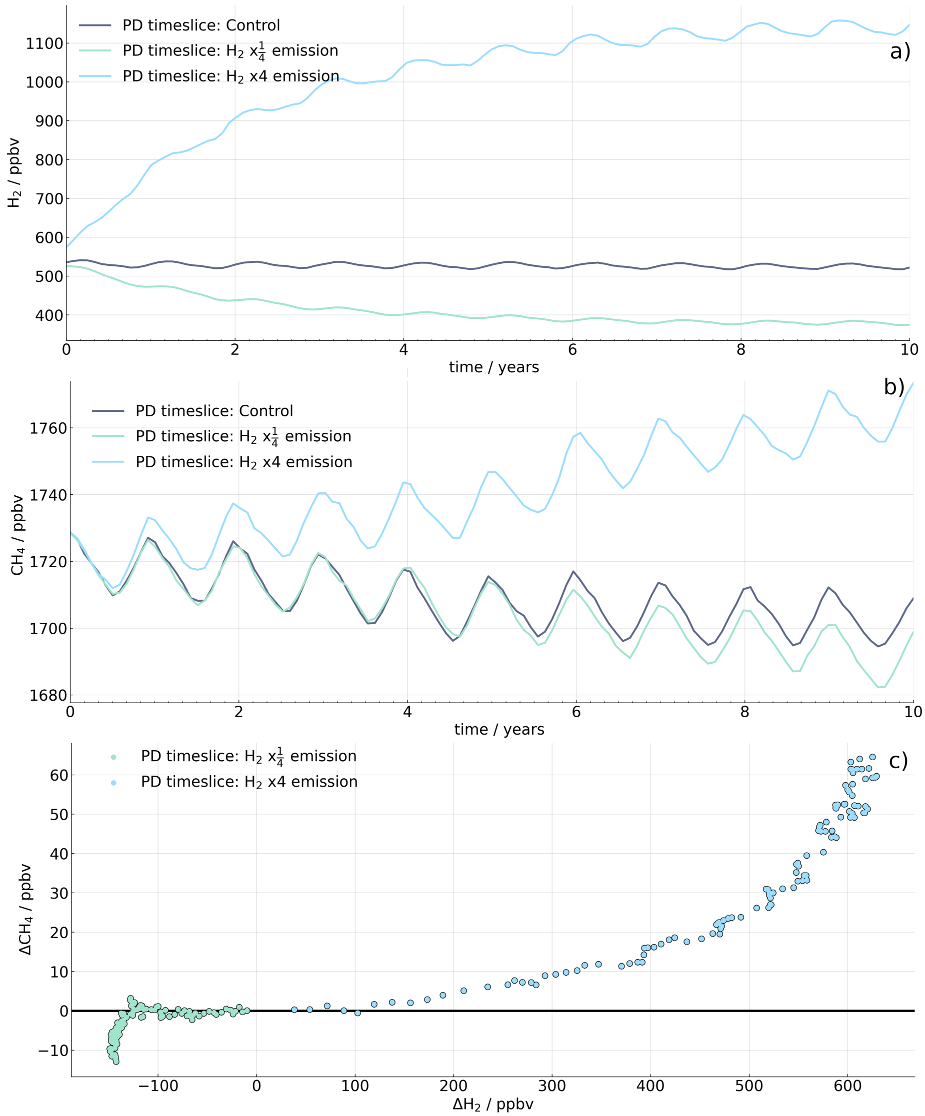

**Figure 9.** Global monthly averaged a) $H_2$ and b) $CH_4$ surface mixing ratios of the (dark blue) control, (green) $\frac{1}{4}$ $H_2$ emissions, and (light blue). c) Difference between the control PD timeslice and the perturbed $H_2$ emissions simulations (perturbed emissions – control). Black line indicates no difference from the control. Timeslices are for 2020.

### 4.3 $H_2$ and $CH_4$ Budget

Both the hydrogen and methane lifetimes calculated in this work include the burden of the whole atmosphere. The hydrogen lifetimes and burdens are summarised in Table 2, while the methane lifetime for the nudged simulations is summarised in Table 3. Budget for the PI and PD timeslices are discussed in Section 4.4.

Hydrogen lifetime is similar between all simulations, ranging between $2.41-2.48$ years. The soil lifetime remains constant, while the lifetime from chemical loss reactions fluctuates between $7.01-7.73$ years. Soil lifetime is expected to produce similar values between all runs, as the deposition is calculated through soil properties and is independent of hydrogen. In Sand et al. (2023), soil lifetime was estimated from prescribed $H_2$ LBC values and both the soil and total model-averaged hydrogen lifetimes are similar to values in this work.

~~The changes between methane lifetime via OH loss are minimal, as shown in Table 3.~~ Methane lifetime decreases when ~~adding in~~ including methane flux (0.167 years; 2.1%), due to the slightly lower abundance of methane than the ~~fixed LBC condition~~LBC condition. This will reduce the feedback on $CH_4$, which is consistent with the findings from Folberth et al. (2022). The changes between methane lifetime via OH loss are minimal, as shown in Table 3. When implementing $H_2$ flux into the ESM with a fixed $CH_4$ LBC, there is a small increase in methane lifetime. This is in agreement with the work conducted in Warwick et al. (2023), who ran a series of experiments with increasing $H_2$ LBC to assess the impact on methane. They found that when hydrogen abundance increased, the methane lifetime via OH reaction increased.

When comparing the $CH_4$ flux simulations with and without $H_2$ flux, however, there is no ~~significant~~ difference in methane lifetime (both are 7.75 years to 2 decimal places). Further to this, the global methane ~~concentration~~ mixing ratio decreases by 25 ppbv. This ~~suggests that the coupling of both interactive hydrogen and methane may cause a decrease in the methane lifetime. Note, however, that these changes in methane lifetime are very small, and a more rigorous experiment should be conducted to confirm these results~~difference in global surface methane mixing ratio is due to the spatial distribution of $H_2$ from the different methodologies (e.g. interactive flux and fixed LBC), and is therefore difficult to directly compare against. Table 3 also shows the $CH_4$ lifetime via OH loss for the present day timeslices with adjusted $H_2$ emissions. The TS-$H_2CH_4$-0.25 simulation which has lower $H_2$ emissions is 0.12 years lower than the present day control, while the TS-$H_2CH_4$-4 with increased $H_2$ emissions has an increased $CH_4$ lifetime of 0.43 years. Given that these differences are larger than in the nudged simulations and are not obscured by different methodologies (all present day timeslices have both $H_2$ and $CH_4$ interactive flux), the response of $CH_4$ to an increase in $H_2$ is in agreement with Warwick et al. (2023).

### 4.4 Pre-industrial and Present Day $H_2$

One application of the combined $CH_4$-$H_2$ emissions driven capability is to explore drivers of the combined $CH_4$-$H_2$ evolution over the industrial period. The links between the two species provide a new opportunity for joint constraints on uncertainty in the emissions and sinks of these two gases. The pre-industrial simulation run from 1850 (~~H~~TS-$H_2$~~;~~ $CH_4$-PI) has a much lower hydrogen burden of ~~129.4~~136.0 Tg than present day (PD) simulations due to having very low anthropogenic emissions. Despite this, the overall hydrogen lifetime is still in line with other present day simulations ~~. This suggests that the increase in hydrogen~~

**Table 2.** Hydrogen lifetime and budget of different simulations. Present day and pre-industrial timeslices are averaged over the last 5 years, nudged runs are averaged between 2008 – 2013. Lifetime is given in years. Burden is in Tg, while chemical production, chemical loss, and emissions are given in Tg $yr^{-1}$.

| Name | $H_2$ total lifetime | $H_2$ soil lifetime | $H_2$ chemical lifetime | Burden | $H_2$ soil loss | $H_2$ atm loss | $H_2$ atm prod | Emissions |
|---|---|---|---|---|---|---|---|---|
| ~~H~~TR-$H_2$-flux | 2.45 | 3.68 | 7.30 | 196.0 | 53.3 | 26.9 | 45.9 | 31.7 |
| ~~H~~TR-$H_2$~~;~~ $CH_4$-flux | 2.46 | 3.68 | 7.45 | 193.2 | 52.5 | 25.9 | 44.4 | 31.7 |
| ~~H~~TS-$H_2$~~;~~ $CH_4$-PI | 2.48 | 3.64 | 7.73 | 136.0 | ~~35.5~~ 37.2 | ~~16.7~~ 17.6 | ~~16.2~~ 31.5 | 18.2 |
| ~~H~~TS-$H_2$~~;~~ $CH_4$-PD | 2.41 | 3.67 | 7.01 | 193.8 | 52.9 | 27.6 | 47.5 | 30.4 |
| Model-average from Sand et al. (2023) | 2.4 | 3.6 | 7.7 | 191 | 57 | 25 | 47 | 36 |
| Average from Surawski et al. (2025) | 2.5 | - | 9.6 | 199.6 | 60.5 | 19.0 | 49.5 | 29.6 |
| Average from Ehhalt and Rohrer (2009) | 2.0 | - | - | 155[1] | 60 | 19 | 41 | 35 |

[1] This is tropospheric $H_2$ burden.

~~emissions has a minimal impact on the loss terms, primarily due to soil uptake being independent of hydrogen in this model.~~ (2.48 years; Table 2).

Figure 10 shows the hemispherically-averaged surface hydrogen and methane ~~concentration~~ mixing ratio from the a) PI (~~H~~TS-$H_2$~~;~~ $CH_4$-PI) and b) ~~present day (PD ) simulation (H~~PD simulation (TS-$H_2$~~;~~ $CH_4$-PD). The PI simulated surface methane ~~concentration~~ mixing ratio (Figure 10a) does not have a strong gradient between hemispheres. Using ice core data from Antarctica and Greenland, Etheridge et al. (1998) showed there was a 24 ppbv discrepancy between hemispheres in the 1850s; with southern hemisphere at 785 ppbv and northern hemisphere values at 809 ppbv. The ~~H~~TS-$H_2$~~;~~ $CH_4$-PI simulation has an an-

**Table 3.** Methane lifetime via OH loss in years from four nudged simulations ~~,~~ (averaged over ~~10~~5 years between 2008 – 2013) and three PD timeslices (averaged over the last 5 years of the 10 year simulation) to 3sf.

| Name | $CH_4$ lifetime via OH (yrs) |
|---|---|
| $H_2$ LBC~~;~~, $CH_4$ LBC (Control) | 7.92 |
| ~~H~~TR-$H_2$~~flux; $CH_4$ LBC~~ -flux | 7.95 |
| ~~$H_2$ LBC; CH~~TR-$CH_4$~~flux~~ -flux | 7.75 |
| ~~H~~TR-$H_2$~~flux;~~ $CH_4$~~flux~~ -flux | 7.75 |
| TS-$H_2$$CH_4$-PD | 7.56 |
| TS-$H_2$$CH_4$-0.25 | 7.44 |
| TS-$H_2$$CH_4$-4 | 7.99 |

nual average of 761 ppbv (SH) and 765 ppbv (NH). Both hemispheres have overlapping inter-annual variability (1 standard deviation), indicating there is no significant difference between hemispheres.

Hydrogen in the northern hemisphere has a strong seasonal cycle and ranges between 405 ppbv (March) to 360 ppbv (October) due to the strong deposition seasonality (as seen in Figure 2). In the southern hemisphere, the surface ~~concentration~~ mixing ratio remains consistent between 372 – 375 ppbv. The southern hemisphere hydrogen ~~concentrations~~ mixing ratios can be compared directly with hydrogen ~~concentrations~~ mixing ratios reconstructed from firn air from Antarctica (Patterson et al., 2021). Around 1850s, Patterson et al. (2021) found that hydrogen levels were 330 ± 15 ppbv, which are slightly lower than the modelled ~~concentration from the H~~mixing ratio from the TS-$H_2$~~;~~ $CH_4$-PI simulation. Firn air measurements for the northern hemisphere are only reconstructed back to 1950s, where the hydrogen ~~concentration was $\approx 400 \pm 25$~~ mixing ratio was $\sim 400 \pm 25$ ppbv (Patterson et al., 2023). The annually averaged ~~H~~TS-$H_2$~~;~~ $CH_4$-PI hydrogen ~~concentration~~ mixing ratio in the northern hemisphere is in agreement with the reconstructed firn data from 1950s. It is likely, however, that the hydrogen ~~concentration~~ mixing ratio was lower in the 1850s, similar to that seen in the southern hemisphere. Thus, the simulated hydrogen ~~concentration is~~ values are likely overestimated.

There is a shift in the seasonal cycle of hydrogen in the PI simulation compared to the present day (Figure 10b; note the different axis for hydrogen ~~concentration~~ mixing ratio for PI and PD). In the northern hemisphere, hydrogen concentration peaks around April-May in PD run, while in the PI simulation, hydrogen peaks earlier in the year (March). ~~There is a relative decrease in southern hemisphere emissions in the PI (likely due to reduced biomass burning) compared to the PD simulation.~~ This is likely due to a ~~decrease in soil uptake seasonality amplitude (PI: 4 Tg yr$^{-1}$ compared to PD: 9 Tg yr$^{-1}$), and a more consistent production of hydrogen throughout the year (PI: 0.17 mol s$^{-1}$ range compared to 0.3 mol s$^{-1}$ range). This combination of a change in production and soil loss~~ smaller chemical source in the summer in the TS-$H_2$$CH_4$-PI simulation, where production only reaches up to 0.38 mol s-1 compared to 0.57 mol s-1 in the TS-$H_2$$CH_4$-PD simulation. The smaller chemical production results in a shift in the ~~northern hemisphere seasonality. Further to this, there is a shift in the hemispheric gradient (Figure 10c), with the hydrogen abundance in the northern hemisphere of the PI simulation greater than the southern hemisphere between~~

~~December-July. The reduced interhemispheric gradient is due to a difference in the balance between northern and southern hydrogen emissions.~~

~~Five-year hemispherical averages of surface hydrogen (blue) and methane (red) mixing ratios for a) 1850 (H2;CH4-PI simulation) and b) 2020 (H2;CH4-PD simulation). Dashed lines show the northern hemisphere, while dotted lines show the southern. Shaded areas show one standard deviation calculated from the last five years of the simulation. c) Zonally averaged surface hydrogen concentration for (blue) PI and (green) PD simulations (averaged over give years).~~

### 4.5 ~~Pulse Experiment~~

~~In addition to the PI simulation, a present dayhydrogen pulse experiment was conducted. Perturbation lifetime is a metric used to measure how much feedback a species would have on its own lifetime if its concentration increased. A feedback factor of 1 indicates that a species lifetime is independent of its own concentration. Perturbation lifetime is calculated by multiplying the atmospheric lifetime of hydrogen from the H~~peak of surface $H_2$ ~~; $CH_4$-PD by the feedback factor. In thisexperiment, the feedback factor is calculated using the 6 years of decay from the H~~mixing ratio to earlier in the year, relative to the present day. Further to this, there is a relative decrease in southern hemisphere emissions in the TS-$H_2$~~;~~ $CH_4$~~-Pulse experiment:~~

~~$\tau_P = \frac{\tau_L}{1-s}$~~

~~where $\tau_P$ is the perturbation lifetime, $\tau_L$ is the steady state atmospheric lifetime from the H~~-PI simulation (due to reduced biomass burning) compared to the TS-$H_2$~~;~~ $CH_4$-PD ~~experiment, and $s$ is the sensitivity coefficient given by:~~

~~$s = \frac{\delta(ln(\tau_L))}{\delta(ln(B))}$~~

~~and $B$ is the burden of the whole atmosphere, and the $\delta(ln(\tau_L))$ used is the change in $H_2$ lifetime from the start of the $H_2$; $CH_4$-Pulse experiment to the end of the 6 years.~~

~~Hydrogen concentration at all altitudes and latitudes was set to 662.5 ppbv globally; a 25% increase from the global-averaged surface concentration (see Methods section for more detail). Increasing the hydrogen concentration in all grid boxes of the model allows for immediate response of CH4 to increased H2 as the hydrogen is already well mixed in the atmosphere. Figure **??** shows the surface response of the system for 6 years after the pulse of hydrogen has been initiated. The dark blue line shows the response, while the green is the control. The perturbation lifetime is calculated as 2.5 years, with a feedback factor of 1.04. This result is in agreement with **?**, who also found that conducting hydrogen pulse emissions both across the globe and at specific locations did not have a significant impact on the hydrogen lifetime (and thus the global warming potential (GWP)). The calculated feedback factor is slightly above the average in Sand et al. (2023), who had a feedback factor of 1.0, but did not have interactive hydrogen and methane at the surface~~simulation, resulting in a smaller difference in hydrogen mixing ratios between hemispheres when comparing between PI and PD scenarios (Figure 10c). Overall, there is a lower seasonal amplitude

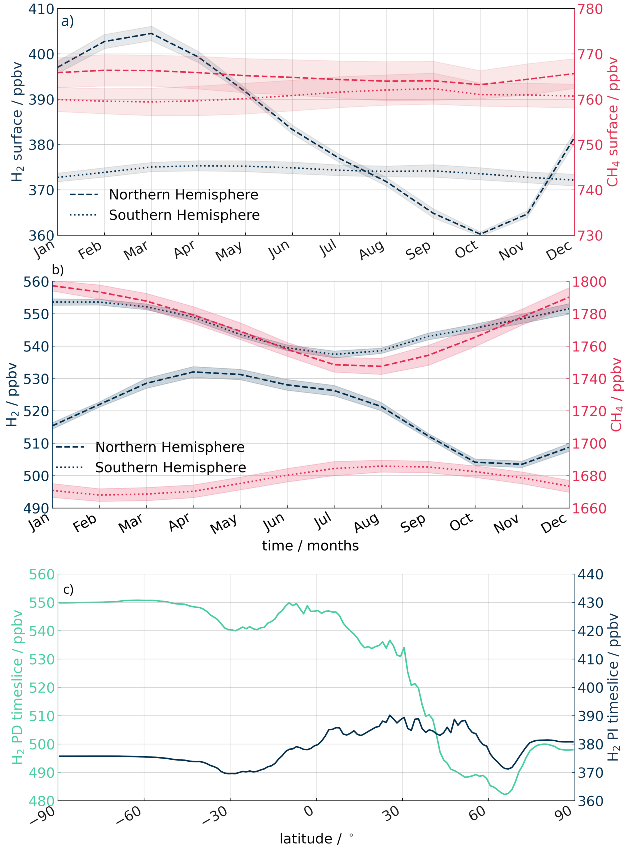

**Figure 10.** ~~Global average~~ Five-year hemispherical averages of surface hydrogen ~~burden for~~ (blue) ~~pulse experiment~~ and methane (~~green~~red) mixing ratios for a) 1850 (TS-$H_2CH_4$-PI simulation) and b) 2020 ~~timeslice~~ (TS-$H_2CH_4$-PD simulation). Dashed lines show the northern hemisphere, while dotted lines show the southern. Shaded areas show one standard deviation calculated from the last five years of the simulation. c) Zonally averaged surface hydrogen mixing ratio for ~~6~~ (blue) PI and (green) PD simulations (averaged over give years).

in the southern hemisphere in the PI scenario due to a smaller seasonal amplitude in the hydrogen chemical production (PI: $0.06\,\text{mol s}^{-1}$ with PD: $0.26\,\text{mol s}^{-1}$), as well as there being no anthropogenic emissions in the PI scenario.

## 5 Conclusions

Hydrogen and methane are closely coupled species in the atmosphere, with both tracers competing for OH as their main atmospheric destruction pathway. We have implemented a hydrogen soil sink scheme into an ESM, along with adding the methane flux from Folberth et al. (2022) to create a fully coupled $H_2$-$CH_4$ ESM. Implementing $H_2$ flux caused the global average surface hydrogen to equilibrate to $540-550$ ppbv, which has been tuned via the soil sink (see Appendix A) to literature values of the tropospheric hydrogen burden (Ehhalt and Rohrer, 2009). The model was able to capture the hydrogen seasonal cycle, which is dominant in the northern hemisphere and is primarily driven by the soil sink.

The inclusion of both $H_2$ flux and $CH_4$ flux had a minimal impact on the overall OH ~~and ozone concentrations~~ concentration and ozone mixing ratio in the model, and there was little change in hydrogen ~~concentration~~ mixing ratios when $CH_4$ ~~flux was added~~LBC was replaced with $CH_4$ flux. Hydrogen and methane mixing ratios were compared against observations at a northern site (Mace Head) and a southern site (Cape Grim). ~~Overall~~In general, both species were found to capture the magnitude and the seasonal cycle of the observations when $H_2$ flux and $CH_4$ flux were on.

When implementing $H_2$ flux into the ESM with $CH_4$ flux, we found methane lifetime remained the same and the overall ~~concentration~~ global surface mixing ratio of methane decreased. This ~~occurred across all latitudes, with a larger decrease~~ decrease is due to the change in the spatial distribution of hydrogen at the surface when switching from fixed $H_2$ LBC to $H_2$ flux, the former of which has no spatial variability. With the replacement of $H_2$ LBC to $H_2$ flux, the overall global surface hydrogen mixing ratio increased. However, the hydrogen mixing ratio decreased in the northern hemisphere ~~.~~ as a result of the soil sink, which led to a decrease in the $CH_4$ lifetime via OH, and a lower global surface $CH_4$ mixing ratio.

When $H_2$ flux and $CH_4$ flux are included, the ESM is able to simulate PI conditions which are within a similar order of magnitude as concentrations found in firn measurements. The seasonal cycle of hydrogen in the PI simulation shifted and peaked earlier in the year, and the gradient between northern and southern ~~concentrations~~ mixing ratio was much smaller, with the hydrogen ~~concentration~~ mixing ratio in the north exceeding that of the south between December-July. ~~Further to this, a hydrogen pulse experiment was conducted and a hydrogen feedback factor of 1.04 was found.~~

These initial experiments show the potential of a fully interactive hydrogen and methane model. Coupling $H_2$ flux and $CH_4$ flux into the ESM allowed the impact of hydrogen on methane to be analysed, and was found to cause a small global decrease in methane. ~~This unexpected~~ A further set of experiments perturbing $H_2$ emissions in a present day timeslice showed a similar response as Warwick et al. (2023), where an increase in $H_2$ results in an increase of $CH_4$. The small decrease in $CH_4$ in the nudged simulations when replacing a fixed $H_2$ LBC with a $H_2$ flux is, therefore, due to comparing different methodologies of surface interactions (interactive flux versus fixed boundary layer). This behaviour highlights the importance of having a fully coupled hydrogen and methane model to further understand their interaction and, ultimately, provide a better estimate of their GWP in present day and future scenarios.

*Code and data availability.* The NOAA methane and hydrogen data is available from https://www.gml.noaa.gov/dv/iadv/ (last accessed: 5th June, 2025). Data from all simulations is found at Brown (2025).

All simulations used in this work were performed using version 12.0 of the Met Office Unified Model coupled to the United Kingdom Chemistry and Aerosol model (UM–UKCA).The UM code branch used in the publication have not all been submitted for review and inclusion in the UM trunk or released for general use. However, the UM and JULES code branches were made available to reviewers of this paper. Due to intellectual property copyright restrictions, we cannot provide the source code for UM–UKCA. The UM–UKCA model is available for use through a licensing agreement. A number of research organisations and national meteorological services use UM–UKCA in collaboration with the Met Office to undertake basic atmospheric process research, produce forecasts, develop the model code, and build and evaluate Earth system models. Please visit https://www.metoffice.gov.uk/research/approach/modelling-systems/unified-model (last accessed: 5th June 2025) for further information on how to apply for a licence.

# Appendix A

## A1 Hydrogen Deposition Scheme

These equations are adapted from Ehhalt and Rohrer (2013) and Paulot et al. (2021). The equation for hydrogen deposition velocity, $v_d(\mathrm{H_2})$ (also known as $\frac{1}{\mathrm{rc}}$), is given by,

$$v_d(\mathrm{H_2}) = \frac{1}{\frac{\delta}{D_s} + \frac{\delta_{\mathrm{snow}}}{D_{\mathrm{snow}}} + \frac{1}{\sqrt{D_s k_s \Theta_a}}} \tag{A1}$$

The deposition scheme can be divided up into three terms; the first describes soil diffusivity where $\delta$ is the soil depth, and $D_s$ is the gas diffusivity of hydrogen into the soil. The second is similar, but describes the diffusion through snow; $\delta_{\mathrm{snow}}$ is the snow depth and $D_{\mathrm{snow}}$ is the gas diffusivity of hydrogen through snow. The third term, $k_s\Theta_a$, describes the microbial uptake and can be split into multiple equations. The gas diffusivity of hydrogen is given as:

$$D_s = \frac{\Theta_a^{3.1} \cdot D_a}{\Theta_p^2} \tag{A2}$$

$\Theta_a$ is the volumetric air fraction (m$^3$ air / m$^3$ total pore space), $\Theta_p$ is the soil porosity (m$^3$ total pore space / m$^3$ total volume). $D_a$ is given by:

$$D_a = 0.611 \cdot \frac{1013.25}{p} \cdot \left(\frac{T + 273.15}{273.15}\right)^{1.75} \tag{A3}$$

$p$ is surface pressure (hPa) and $T$ is soil temperature (°C). $k_s\Theta_a$ can be broken down into three functions:

$$k_s\Theta_a = A \cdot f(\Theta_a) \cdot g(T_s) \tag{A4}$$

$A$ is a scaling factor and is used as a proxy for microbial activity:

$$A = \alpha \frac{\mathrm{soil_C}}{\beta + \mathrm{soil_C}} \tag{A5}$$

where $\mathrm{soil_C}$ is the soil carbon content and $\beta = 7\,\mathrm{kgC\ m^{-3}}$ as per Paulot et al. (2021). $\alpha$ is a unitless parameter, which was set to 30 by scaling the tropospheric hydrogen global burden to approximately 155 Tg and, thus, inline with results from Ehhalt and Rohrer (2009). The ~~$g(T_s)$~~ $g(T)$ term from Equation A4 is given by:

$$g(T_s) = \frac{1}{1+\exp(-\frac{T-3.8}{6.7})} + \frac{1}{1+\exp(\frac{T-62.2}{7.1})} - 1 \tag{A6}$$

while the $f(\Theta_a)$ function is dependent on the soil type. For sand, the equation is given by:

$$f_s(\Theta_a) = 0.00936 \cdot \frac{(\frac{\Theta_w}{\Theta_p} - 0.02640)\cdot(1-\frac{\Theta_w}{\Theta_p})}{(\frac{\Theta_w}{\Theta_p})^2 - 0.1715\cdot(\frac{\Theta_w}{\Theta_p}) + 0.03144} \tag{A7}$$

where $\Theta_a = \frac{\Theta_w}{\Theta_p}$, and $\Theta_w$ and $\Theta_p$ are the volumetric soil moisture content (SMC) and the total porosity respectively, with limits;

$$\Theta_p \geq 1 \tag{A8}$$

$$\Theta_w \geq 0.0264 \tag{A9}$$

For loam, $\Theta_a$ is:

$$f_l(\Theta_a) = 0.01997 \cdot \frac{(\frac{\Theta_w}{\Theta_p} - 0.05369)\cdot(0.8508-\frac{\Theta_w}{\Theta_p})}{(\frac{\Theta_w}{\Theta_p})^2 - 0.7541\cdot(\frac{\Theta_w}{\Theta_p}) + 0.2806} \tag{A10}$$

The limits for $f_l(\Theta_a)$ are:

$$\Theta_p \geq 0.851 \tag{A11}$$

$$\Theta_w \geq 0.0537 \tag{A12}$$

**Table A1.** NOAA observation site for hydrogen divided into north and south. Numbers correspond to the values even in the Taylor diagram (Figure 5). Values with * do not appear on the Taylor diagram due to either having a negative correlation, or a normalised standard deviation greater than 2

| Site number (N) | Name (N) | Years | Site Number (S) | Name (S) | Years |
|---|---|---|---|---|---|
| 1 | h2 ask surface-flask 1 ccgg event | 2009-2013 | 1 | h2 crz surface-flask 1 ccgg event | 2009-2013 |
| 2 | h2 bal surface-flask 1 ccgg event | 2009-2011 | 2 | h2 bkt surface-flask 1 ccgg event | 2009-2013 |
| 3 | h2 llb surface-flask 1 ccgg event | 2009-2013 | 3 | h2 cpt surface-flask 1 ccgg event | 2010-2013 |
| 4 | h2 dsi surface-flask 1 ccgg event | 2010-2013 | 4 | h2 asc surface-flask 1 ccgg event | 2009-2013 |
| 5 | h2 brw surface-flask 1 ccgg event | 2009-2013 | 5 | h2 bhd surface-flask 1 ccgg event | 2009-2013 |
| 6 | h2 pal surface-flask 1 ccgg event | 2009-2013 | 6 | h2 sey surface-flask 1 ccgg event | 2009-2013 |
| 7 | h2 nwr surface-flask 1 ccgg event | 2009-2013 | 7 | h2 psa surface-flask 1 ccgg event | 2009-2013 |
| 8 | h2 wis surface-flask 1 ccgg event | 2009-2013 | 8 | h2 drp shipboard-flask 1 ccgg event | 2009-2013 |
| 9 | h2 sdz surface-flask 1 ccgg event* | 2009-2013 | 9 | h2 mkn surface-flask 1 ccgg event | 2009-2011 |
| 10 | h2 bsc surface-flask 1 ccgg event | 2009-2011 | 10 | h2 spo surface-flask 1 ccgg event | 2009-2013 |
| 11 | h2 sgp surface-flask 1 ccgg event | 2009-2013 | 11 | h2 hba surface-flask 1 ccgg event | 2009-2013 |
| 12 | h2 azr surface-flask 1 ccgg event | 2007-2013 | 12 | h2 nat surface-flask 1 ccgg event | 2010-2013 |
| 13 | h2 hsu surface-flask 1 ccgg event | 2010-2013 | 13 | h2 nmb surface-flask 1 ccgg event | 2009-2013 |
| 14 | h2 uum surface-flask 1 ccgg event | 2009-2013 | 14 | h2 smo surface-flask 1 ccgg event | 2009-2013 |
| 15 | h2 tik surface-flask 1 ccgg event | 2011-2013 | 15 | h2 cgo surface-flask 1 ccgg event | 2009-2013 |
| 16 | h2 thd surface-flask 1 ccgg event | 2009-2013 | 16 | h2 ush surface-flask 1 ccgg event | 2009-2013 |
| 17 | h2 cib surface-flask 1 ccgg event | 2009-2013 | 17 | h2 syo surface-flask 1 ccgg event | 2009-2013 |
| 18 | h2 uta surface-flask 1 ccgg event | 2009-2013 | 18 | h2 eic surface-flask 1 ccgg event | 2009-2013 |
| 19 | h2 chr surface-flask 1 ccgg event | 2009-2013 | - | - | - |
| 20 | h2 mlo surface-flask 1 ccgg event* | 2009-2013 | - | - | - |
| 21 | h2 key surface-flask 1 ccgg event | 2009-2013 | - | - | - |
| 22 | h2 izo surface-flask 1 ccgg event | 2009-2013 | - | - | - |
| 23 | h2 wpc shipboard-flask 1 ccgg event | 2009-2013 | - | - | - |
| 24 | h2 poc shipboard-flask 1 ccgg event | 2009-2012 | - | - | - |
| 25 | h2 oxk surface-flask 1 ccgg event* | 2009-2013 | - | - | - |

**Table A1.** Cont.

| Site number (N) | Name (N) | Years | Site Number (S) | Name (S) | Years |
|---|---|---|---|---|---|
| 26 | h2 alt surface-flask 1 ccgg event* | 2009-2013 | - | - | - |
| 27 | h2 bmw surface-flask 1 ccgg event | 2009-2013 | - | - | - |
| 28 | h2 rpb surface-flask 1 ccgg event | 2009-2013 | - | - | - |
| 29 | h2 hun surface-flask 1 ccgg event* | 2009-2013 | - | - | - |
| 30 | h2 tap surface-flask 1 ccgg event | 2009-2013 | - | - | - |
| 31 | h2 shm surface-flask 1 ccgg event | 2009-2013 | - | - | - |
| 32 | h2 mex surface-flask 1 ccgg event | 2009-2013 | - | - | - |
| 33 | h2 sum surface-flask 1 ccgg event | 2009-2013 | - | - | - |
| 34 | h2 ice surface-flask 1 ccgg event | 2009-2013 | - | - | - |
| 35 | h2 hpb surface-flask 1 ccgg event | 2009-2013 | - | - | - |
| 36 | h2 lmp surface-flask 1 ccgg event | 2009-2013 | - | - | - |
| 37 | h2 pta surface-flask 1 ccgg event | 2009-2011 | - | - | - |
| 38 | h2 kum surface-flask 1 ccgg event | 2009-2013 | - | - | - |
| 39 | h2 cba surface-flask 1 ccgg event | 2009-2013 | - | - | - |
| 40 | h2 mid surface-flask 1 ccgg event | 2009-2013 | - | - | - |
| 41 | h2 mhd surface-flask 1 ccgg event | 2009-2013 | - | - | - |
| 42 | h2 wlg surface-flask 1 ccgg event | 2009-2013 | - | - | - |
| 43 | h2 zep surface-flask 1 ccgg event | 2009-2013 | - | - | - |
| 44 | h2 lln surface-flask 1 ccgg event | 2009-2013 | - | - | - |

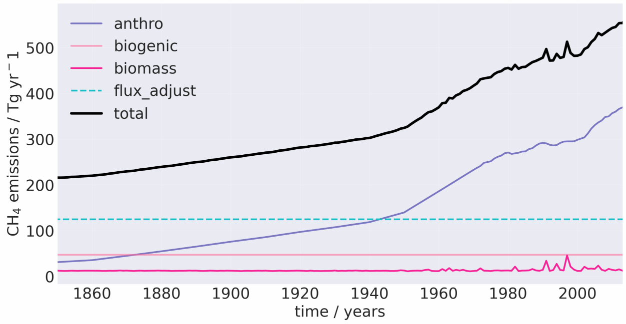

**Figure A1.** Yearly, globally averaged methane emissions from $1850-2014$ (excluding wetlands). The flux adjustment is that used in the nudged simulations and is a total $124\ \mathrm{CH_4\ Tg\ yr^{-1}}$.

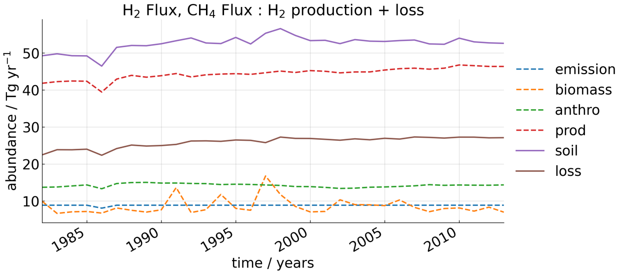

**Figure A2.** Globally averaged hydrogen sources and sinks from 1982 − 2013. 'emissions' refers to the natural hydrogen emissions both from the ocean and land. 'prod' and 'loss' refers to the atmospheric chemical production and loss of $H_2$ respectively.

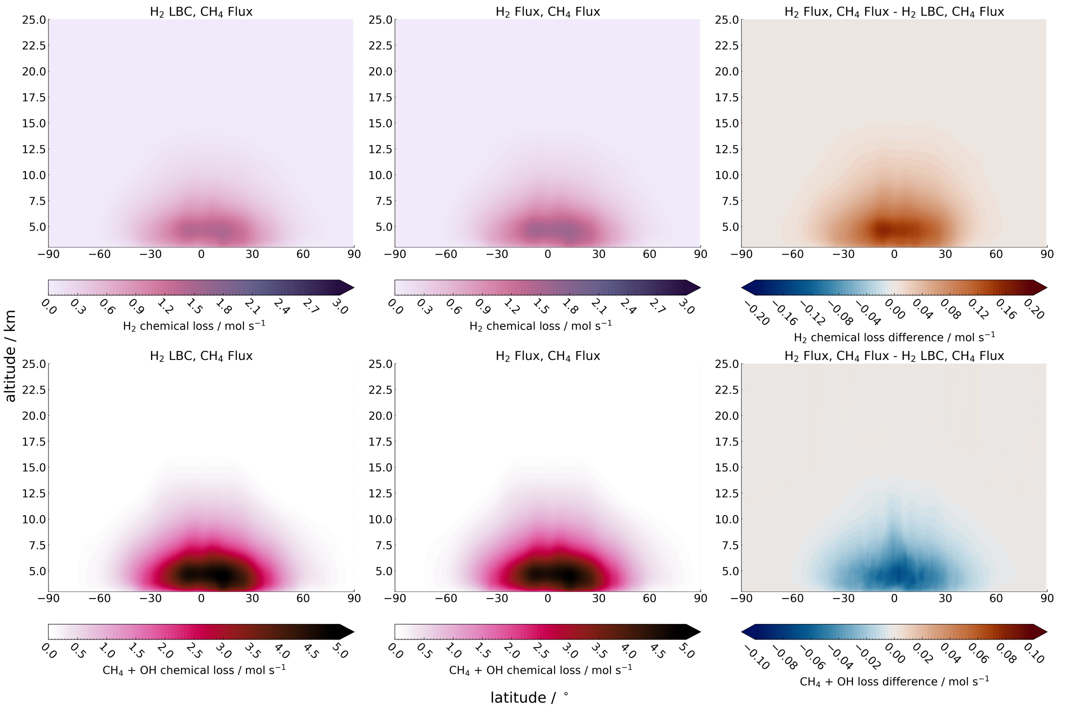

**Figure A3.** Zonally averaged (top) H$_2$ chemical loss and (bottom) CH$_4$ loss via OH for (left) ~~CH~~TR-CH$_4$-flux simulation, (middle) ~~H~~TR-H$_2$~~;~~ CH$_4$-flux simulation, and (right) difference between the two (CH$_4$-flux − ~~H~~TR-H$_2$~~;~~ CH$_4$-flux) averaged between 2008 – 2013. Red (blue) shows an increase (decrease) from the ~~CH~~TR-CH$_4$-flux. Note the non-linearity of scales.

~~Zonally averaged reaction rate of kHO$_2$NOfor (left) CH$_4$-flux simulation, (middle) H$_2$; CH$_4$-flux simulation, and (right) difference between the two (CH$_4$-flux — H$_2$; CH$_4$-flux) averaged between 2008 — 2013. Red (blue) shows a increase (decrease) from the CH$_4$-flux.~~

*Author contributions.* MAJB ran the simulations, analysed the data and wrote the manuscript. ATA and NJW helped with the analysis, ideas, and proofread the manuscript. PTG helped with ideas and proofread the manuscript. NLA set up and provided the models for all simulations and proofread the manuscript. STR produced the hydrogen emissions needed for $H_2$ flux simulations and contributed to the methods section. GAF and FMO provided the $CH_4$ flux emissions files setup, helped with analysis and proofread the manuscript. HB helped with the initial hydrogen settings, helped with the analysis and proofread the manuscript.

*Competing interests.* There are no competing interests present in this work.

*Acknowledgements.* MB, NJW, NLA, and ATA were supported by the National Environment Research Council through grand NE/X010236/1. F.M. O'Connor and G.A. Folberth were supported by the Met Office Hadley Centre Climate Programme funded by DSIT and through the EU Horizon project ESM2025 (Grant 101003536). This work used JASMIN, the UK collaborative data analysis facility. This work used the ARCHER2 UK National Supercomputing Service (https://www.archer2.ac.uk) (Beckett et al., 2024). We acknowledge use of the Monsoon2 system, a collaborative facility supplied under the Joint Weather and Climate Research Programme, a strategic partnership between the Met Office and the Natural Environment Research Council.

## References

Archibald, A. T., O'Connor, F. M., Abraham, N. L., Archer-Nicholls, S., Chipperfield, M. P., Dalvi, M., Folberth, G. A., Dennison, F., Dhomse, S. S., Griffiths, P. T., Hardacre, C., Hewitt, A. J., Hill, R. S., Johnson, C. E., Keeble, J., Köhler, M. O., Morgenstern, O., Mulcahy, J. P., Ordóñez, C., Pope, R. J., Rumbold, S. T., Russo, M. R., Savage, N. H., Sellar, A., Stringer, M., Turnock, S. T., Wild, O., and Zeng, G.: Description and evaluation of the UKCA stratosphere–troposphere chemistry scheme (StratTrop vn 1.0) implemented in UKESM1, Geoscientific Model Development, 13, 1223–1266, https://doi.org/10.5194/gmd-13-1223-2020, 2020.

Beckett, G., Beech-Brandt, J., Leach, K., Payne, Z., Simpson, A., Smith, L., Turner, A., and Whiting, A.: ARCHER2 Service Description, https://doi.org/10.5281/zenodo.14507040, 2024.

Belviso, S., Schmidt, M., Yver, C., Ramonet, M., Gros, V., and Launois, T.: Strong similarities between night-time deposition velocities of carbonyl sulphide and molecular hydrogen inferred from semi-continuous atmospheric observations in Gif-sur-Yvette, Paris region, Tellus B: Chemical and Physical Meteorology, 65, 20 719, https://doi.org/10.3402/tellusb.v65i0.20719, 2013.

Bertagni, M. B., Paulot, F., and Porporato, A.: Moisture fluctuations modulate abiotic and biotic limitations of H2 soil uptake, Global Biogeochemical Cycles, 35, e2021GB006 987, https://repository.library.noaa.gov/view/noaa/46421, 2021.

Brown, M. A. J.: Dataset: Development of Fully Interactive Hydrogen with Methane in UKESM1.0, https://doi.org/10.5281/zenodo.15574652, 2025.

Brown, M. A. J., Warwick, N. J., and Archibald, A. T.: Multi-Model Assessment of Future Hydrogen Soil Deposition and Lifetime Using CMIP6 Data, Geophysical Research Letters, 52, e2024GL113 653, https://doi.org/https://doi.org/10.1029/2024GL113653, e2024GL113653 2024GL113653, 2025.

Bryant, H. N., Stevenson, D. S., Heal, M. R., and Abraham, N. L.: Impacts of hydrogen on tropospheric ozone and methane and their modulation by atmospheric NOx, Frontiers in Energy Research, 12, https://doi.org/10.3389/fenrg.2024.1415593, 2024.

Chen, C., Solomon, S., and Stone, K.: On the chemistry of the global warming potential of hydrogen, Frontiers in Energy Research, 12, https://doi.org/10.3389/fenrg.2024.1463450, 2024.

Cowan, N., Roberts, T., Hanlon, M., Bezanger, A., Toteva, G., Tweedie, A., Yeung, K., Deshpande, A., Levy, P., Skiba, U., Nemitz, E., and Drewer, J.: Quantifying the soil sink of atmospheric Hydrogen: a full year of field measurements from grassland and forest soils in the UK, EGUsphere, 2024, 1–21, https://doi.org/10.5194/egusphere-2024-3654, 2024.

Dee, D. P., Uppala, S. M., Simmons, A. J., Berrisford, P., Poli, P., Kobayashi, S., Andrae, U., Balmaseda, M. A., Balsamo, G., Bauer, P., Bechtold, P., Beljaars, A. C. M., van de Berg, L., Bidlot, J., Bormann, N., Delsol, C., Dragani, R., Fuentes, M., Geer, A. J., Haimberger, L., Healy, S. B., Hersbach, H., Hólm, E. V., Isaksen, L., Kållberg, P., Köhler, M., Matricardi, M., McNally, A. P., Monge-Sanz, B. M., Morcrette, J.-J., Park, B.-K., Peubey, C., de Rosnay, P., Tavolato, C., Thépaut, J.-N., and Vitart, F.: The ERA-Interim reanalysis: configuration and performance of the data assimilation system, Quarterly Journal of the Royal Meteorological Society, 137, 553–597, https://doi.org/https://doi.org/10.1002/qj.828, 2011.

Derwent, R., Simmonds, P., O'Doherty, S., Manning, A., Collins, W., and Stevenson, D.: Global environmental impacts of the hydrogen economy, International Journal of Nuclear Hydrogen Production and Applications, 1, 57–67, https://doi.org/10.1504/IJNHPA.2006.009869, 2006.

Dorigo, W., Preimesberger, W., Hahn, S., Van der Schalie, R., De Jeu, R., Kidd, R., Rodriguez-Fernandez, N., Hirschi, M., Stradiotti, P., Frederikse, T., Gruber, A., and Madelon, R.: ESA Soil Moisture Climate Change Initiative: Version 08.1 data collection, NERC EDS Centre for Environmental Data Analysis, date of citation, https://catalogue.ceda.ac.uk/uuid/ff890589c21f4033803aa550f52c980c/, 2023.

Ehhalt, D. H. and Rohrer, F.: The tropospheric cycle of H2: a critical review, Tellus B: Chemical and Physical Meteorology, 61, 500–535, https://doi.org/10.1111/j.1600-0889.2009.00416.x, 2009.

Ehhalt, D. H. and Rohrer, F.: Deposition velocity of H2: a new algorithm for its dependence on soil moisture and temperature, Tellus B: Chemical and Physical Meteorology, 65, 19 904, https://doi.org/10.3402/tellusb.v65i0.19904, 2013.

Etheridge, D. M., Steele, L. P., Francey, R. J., and Langenfelds, R. L.: Atmospheric methane between 1000 A.D. and present: Evidence of anthropogenic emissions and climatic variability, Journal of Geophysical Research: Atmospheres, 103, 15 979–15 993, https://doi.org/https://doi.org/10.1029/98JD00923, 1998.

Folberth, G. A., Staniaszek, Z., Archibald, A. T., Gedney, N., Griffiths, P. T., Jones, C. D., O'Connor, F. M., Parker, R. J., Sellar, A. A., and Wiltshire, A.: Description and Evaluation of an Emission-Driven and Fully Coupled Methane Cycle in UKESM1, Journal of Advances in Modeling Earth Systems, 14, e2021MS002 982, https://doi.org/10.1029/2021MS002982, e2021MS002982 2021MS002982, 2022.

Fung, I., John, J., Lerner, J., Matthews, E., Prather, M., Steele, L. P., and Fraser, P. J.: Three-dimensional model synthesis of the global methane cycle, Journal of Geophysical Research: Atmospheres, 96, 13 033–13 065, https://doi.org/https://doi.org/10.1029/91JD01247, 1991.

Gidden, M. J., Riahi, K., Smith, S. J., Fujimori, S., Luderer, G., Kriegler, E., van Vuuren, D. P., van den Berg, M., Feng, L., Klein, D., Calvin, K., Doelman, J. C., Frank, S., Fricko, O., Harmsen, M., Hasegawa, T., Havlik, P., Hilaire, J., Hoesly, R., Horing, J., Popp, A., Stehfest, E., and Takahashi, K.: Global emissions pathways under different socioeconomic scenarios for use in CMIP6: a dataset of harmonized emissions trajectories through the end of the century, Geoscientific Model Development, 12, 1443–1475, https://doi.org/10.5194/gmd-12-1443-2019, 2019.

Granier, C., Guenther, A., Lamarque, J., Mieville, A., Muller, J., Olivier, J., Orlando, J., Peters, J., Petron, G., Tyndall, G., et al.: POET, a database of surface emissions of ozone precursors available online at: http://www. aero. jussieu. fr/projet/ACCENT, POET. php, 2005.

Hayman, G. D., O'Connor, F. M., Dalvi, M., Clark, D. B., Gedney, N., Huntingford, C., Prigent, C., Buchwitz, M., Schneising, O., Burrows, J. P., Wilson, C., Richards, N., and Chipperfield, M.: Comparison of the HadGEM2 climate-chemistry model against in situ and SCIAMACHY atmospheric methane data, Atmospheric Chemistry and Physics, 14, 13 257–13 280, https://doi.org/10.5194/acp-14-13257-2014, 2014.

Hersbach, H., Bell, B., Berrisford, P., Hirahara, S., Horányi, A., Muñoz-Sabater, J., Nicolas, J., Peubey, C., Radu, R., Schepers, D., Simmons, A., Soci, C., Abdalla, S., Abellan, X., Balsamo, G., Bechtold, P., Biavati, G., Bidlot, J., Bonavita, M., De Chiara, G., Dahlgren, P., Dee, D., Diamantakis, M., Dragani, R., Flemming, J., Forbes, R., Fuentes, M., Geer, A., Haimberger, L., Healy, S., Hogan, R. J., Hólm, E., Janisková, M., Keeley, S., Laloyaux, P., Lopez, P., Lupu, C., Radnoti, G., de Rosnay, P., Rozum, I., Vamborg, F., Villaume, S., and Thépaut, J.-N.: The ERA5 global reanalysis, Quarterly Journal of the Royal Meteorological Society, 146, 1999–2049, https://doi.org/https://doi.org/10.1002/qj.3803, 2020.

Hicks, B., Baldocchi, D., Meyers, T., Hosker, R., and Matt, D.: A preliminary multiple resistance routine for deriving dry deposition velocities from measured quantities, Water, Air, and Soil Pollution, 36, 311–330, 1987.

Hoesly, R. M., Smith, S. J., Feng, L., Klimont, Z., Janssens-Maenhout, G., Pitkanen, T., Seibert, J. J., Vu, L., Andres, R. J., Bolt, R. M., Bond, T. C., Dawidowski, L., Kholod, N., Kurokawa, J.-I., Li, M., Liu, L., Lu, Z., Moura, M. C. P., O'Rourke, P. R., and Zhang, Q.: Historical (1750–2014) anthropogenic emissions of reactive gases and aerosols from the Community Emissions Data System (CEDS), Geoscientific Model Development, 11, 369–408, https://doi.org/10.5194/gmd-11-369-2018, 2018.

Holmes, C. D.: Methane Feedback on Atmospheric Chemistry: Methods, Models, and Mechanisms, Journal of Advances in Modeling Earth Systems, 10, 1087–1099, https://doi.org/https://doi.org/10.1002/2017MS001196, 2018.

Hydrogen Council: Path to hydrogencompetitiveness A cost perspective, Tech. rep., Hydrogen Council, https://doi.org/https://www.h2knowledgecentre.com/content/policypaper1202?crawler=redirect%26mimetype=application/pdf, 2020.

Jordaan, K., Lappan, R., Dong, X., Aitkenhead, I. J., Bay, S. K., Chiri, E., Wieler, N., Meredith, L. K., Cowan, D. A., Chown, S. L., and Greening, C.: Hydrogen-Oxidizing Bacteria Are Abundant in Desert Soils and Strongly Stimulated by Hydration, mSystems, 5, 10.1128/msystems.01 131–20, https://doi.org/10.1128/msystems.01131-20, 2020.

Lallo, M., Aalto, T., Laurila, T., and Hatakka, J.: Seasonal variations in hydrogen deposition to boreal forest soil in southern Finland, Geophysical Research Letters, 35, https://doi.org/https://doi.org/10.1029/2007GL032357, 2008.

Marrero, T. R. and Mason, E. A.: Gaseous Diffusion Coefficients, Journal of Physical and Chemical Reference Data, 1, 3–118, https://doi.org/10.1063/1.3253094, 1972.

Meredith, L. K., Commane, R., Keenan, T. F., Klosterman, S. T., Munger, J. W., Templer, P. H., Tang, J., Wofsy, S. C., and Prinn, R. G.: Ecosystem fluxes of hydrogen in a mid-latitude forest driven by soil microorganisms and plants, Global Change Biology, 23, 906–919, https://doi.org/https://doi.org/10.1111/gcb.13463, 2017.

Patterson, J. D., Aydin, M., Crotwell, A. M., Pétron, G., Severinghaus, J. P., Krummel, P. B., Langenfelds, R. L., and Saltzman, E. S.: $H_2$ in Antarctic firn air: Atmospheric reconstructions and implications for anthropogenic emissions, Proceedings of the National Academy of Sciences, 118, e2103335 118, https://doi.org/10.1073/pnas.2103335118, 2021.

Patterson, J. D., Aydin, M., Crotwell, A. M., Pétron, G., Severinghaus, J. P., Krummel, P. B., Langenfelds, R. L., Petrenko, V. V., and Saltzman, E. S.: Reconstructing atmospheric $H_2$ over the past century from bi-polar firn air records, Climate of the Past, 19, 2535–2550, https://doi.org/10.5194/cp-19-2535-2023, 2023.

Paulot, F., Paynter, D., Naik, V., Malyshev, S., Menzel, R., and Horowitz, L. W.: Global modeling of hydrogen using GFDL-AM4.1: Sensitivity of soil removal and radiative forcing, International Journal of Hydrogen Energy, 46, 13 446–13 460, https://doi.org/https://doi.org/10.1016/j.ijhydene.2021.01.088, 2021.

Pétron, G., Crotwell, A. M., Mund, J., Crotwell, M., Mefford, T., Thoning, K., Hall, B., Kitzis, D., Madronich, M., Moglia, E., Neff, D., Wolter, S., Jordan, A., Krummel, P., Langenfelds, R., and Patterson, J.: Atmospheric $H_2$ observations from the NOAA Cooperative Global Air Sampling Network, Atmospheric Measurement Techniques, 17, 4803–4823, https://doi.org/10.5194/amt-17-4803-2024, 2024.

Pinnington, E., Quaife, T., and Black, E.: Impact of remotely sensed soil moisture and precipitation on soil moisture prediction in a data assimilation system with the JULES land surface model, Hydrology and Earth System Sciences, 22, 2575–2588, https://doi.org/10.5194/hess-22-2575-2018, 2018.

Prinn, R. G., Weiss, R. F., Arduini, J., Arnold, T., DeWitt, H. L., Fraser, P. J., Ganesan, A. L., Gasore, J., Harth, C. M., Hermansen, O., Kim, J., Krummel, P. B., Li, S., Loh, Z. M., Lunder, C. R., Maione, M., Manning, A. J., Miller, B. R., Mitrevski, B., Mühle, J., O'Doherty, S., Park, S., Reimann, S., Rigby, M., Saito, T., Salameh, P. K., Schmidt, R., Simmonds, P. G., Steele, L. P., Vollmer, M. K., Wang, R. H., Yao, B., Yokouchi, Y., Young, D., and Zhou, L.: History of chemically and radiatively important atmospheric gases from the Advanced Global Atmospheric Gases Experiment (AGAGE), Earth System Science Data, 10, 985–1018, https://doi.org/10.5194/essd-10-985-2018, 2018.

Rao, S., Klimont, Z., Smith, S. J., Van Dingenen, R., Dentener, F., Bouwman, L., Riahi, K., Amann, M., Bodirsky, B. L., van Vuuren, D. P., Aleluia Reis, L., Calvin, K., Drouet, L., Fricko, O., Fujimori, S., Gernaat, D., Havlik, P., Harmsen, M., Hasegawa, T., Heyes, C., Hilaire, J., Luderer, G., Masui, T., Stehfest, E., Strefler, J., van der Sluis, S., and Tavoni, M.: Future air pollution in the Shared Socio-economic Pathways, Global Environmental Change, 42, 346–358, https://doi.org/https://doi.org/10.1016/j.gloenvcha.2016.05.012, 2017.

Riahi, K., van Vuuren, D. P., Kriegler, E., Edmonds, J., O'Neill, B. C., Fujimori, S., Bauer, N., Calvin, K., Dellink, R., Fricko, O., Lutz, W., Popp, A., Cuaresma, J. C., KC, S., Leimbach, M., Jiang, L., Kram, T., Rao, S., Emmerling, J., Ebi, K., Hasegawa, T., Havlik, P., Humpenöder, F., Da Silva, L. A., Smith, S., Stehfest, E., Bosetti, V., Eom, J., Gernaat, D., Masui, T., Rogelj, J., Strefler, J., Drouet, L., Krey, V., Luderer, G., Harmsen, M., Takahashi, K., Baumstark, L., Doelman, J. C., Kainuma, M., Klimont, Z., Marangoni, G., Lotze-Campen, H., Obersteiner, M., Tabeau, A., and Tavoni, M.: The Shared Socioeconomic Pathways and their energy, land use, and greenhouse gas emissions implications: An overview, Global Environmental Change, 42, 153–168, https://doi.org/https://doi.org/10.1016/j.gloenvcha.2016.05.009, 2017.

Sand, M., Skeie, R. B., Sandstad, M., Krishnan, S., Myhre, G., Bryant, H., Derwent, R., Hauglustaine, D., Paulot, F., Prather, M., et al.: A multi-model assessment of the Global Warming Potential of hydrogen, Communications Earth & Environment, 4, 203, 2023.

Sanderson, M., Collins, W., Derwent, R., and Johnson, C.: Simulation of global hydrogen levels using a Lagrangian three-dimensional model, Journal of Atmospheric Chemistry, 46, 15–28, 2003.

Sellar, A. A., Walton, J., Jones, C. G., Wood, R., Abraham, N. L., Andrejczuk, M., Andrews, M. B., Andrews, T., Archibald, A. T., de Mora, L., Dyson, H., Elkington, M., Ellis, R., Florek, P., Good, P., Gohar, L., Haddad, S., Hardiman, S. C., Hogan, E., Iwi, A., Jones, C. D., Johnson, B., Kelley, D. I., Kettleborough, J., Knight, J. R., Köhler, M. O., Kuhlbrodt, T., Liddicoat, S., Linova-Pavlova, I., Mizielinski, M. S., Morgenstern, O., Mulcahy, J., Neininger, E., O'Connor, F. M., Petrie, R., Ridley, J., Rioual, J.-C., Roberts, M., Robertson, E., Rumbold, S., Seddon, J., Shepherd, H., Shim, S., Stephens, A., Teixiera, J. C., Tang, Y., Williams, J., Wiltshire, A., and Griffiths, P. T.: Implementation of U.K. Earth System Models for CMIP6, Journal of Advances in Modeling Earth Systems, 12, e2019MS001 946, https://doi.org/https://doi.org/10.1029/2019MS001946, e2019MS001946 10.1029/2019MS001946, 2020.

Simmonds, P., Derwent, R., Mannin, A., Grant, A., O'doherty, S., and Spain, T.: Estimation of hydrogen deposition velocities from 1995-2008 at Mace Head, Ireland using a simple box model and concurrent ozone depositions, Tellus B: Chemical and Physical Meteorology, 63, 40–51, https://doi.org/10.1111/j.1600-0889.2010.00518.x, 2011.

Sindelarova, K., Granier, C., Bouarar, I., Guenther, A., Tilmes, S., Stavrakou, T., Müller, J.-F., Kuhn, U., Stefani, P., and Knorr, W.: Global data set of biogenic VOC emissions calculated by the MEGAN model over the last 30 years, Atmospheric Chemistry and Physics, 14, 9317–9341, https://doi.org/10.5194/acp-14-9317-2014, 2014.

Surawski, N., Steil, B., Brühl, C., Gromov, S., Klingmüller, K., Martin, A., Pozzer, A., and Lelieveld, J.: Global atmospheric hydrogen chemistry and long-term source-sink budget simulation with the EMAC v2.55 model, EGUsphere, 2025, 1–29, https://doi.org/10.5194/egusphere-2025-1559, 2025.

Telford, P. J., Braesicke, P., Morgenstern, O., and Pyle, J. A.: Technical Note: Description and assessment of a nudged version of the new dynamics Unified Model, Atmospheric Chemistry and Physics, 8, 1701–1712, https://doi.org/10.5194/acp-8-1701-2008, 2008.

Tromp, T. K., Shia, R.-L., Allen, M., Eiler, J. M., and Yung, Y. L.: Potential Environmental Impact of a Hydrogen Economy on the Stratosphere, Science, 300, 1740–1742, https://doi.org/10.1126/science.1085169, 2003.

van Marle, M. J. E., Kloster, S., Magi, B. I., Marlon, J. R., Daniau, A.-L., Field, R. D., Arneth, A., Forrest, M., Hantson, S., Kehrwald, N. M., Knorr, W., Lasslop, G., Li, F., Mangeon, S., Yue, C., Kaiser, J. W., and van der Werf, G. R.: Historic global biomass burning emissions for CMIP6 (BB4CMIP) based on merging satellite observations with proxies and fire models (1750–2015), Geoscientific Model Development, 10, 3329–3357, https://doi.org/10.5194/gmd-10-3329-2017, 2017.

Warwick, N. J., Bekki, S., Nisbet, E., and Pyle, J. A.: Impact of a hydrogen economy on the stratosphere and troposphere studied in a 2-D model, Geophysical Research Letters, 31, https://doi.org/https://doi.org/10.1029/2003GL019224, 2004.

Warwick, N. J., Archibald, A. T., Griffiths, P. T., Keeble, J., O'Connor, F. M., Pyle, J. A., and Shine, K. P.: Atmospheric composition and climate impacts of a future hydrogen economy, Atmospheric Chemistry and Physics, https://doi.org/10.1029/2024GL112445, 2023.

Yang, L. H., Jacob, D. J., Lin, H., Dang, R., Bates, K. H., East, J. D., Travis, K. R., Pendergrass, D. C., and Murray, L. T.: Model underestimates of OH reactivity cause overestimate of hydrogen's climate impact, https://arxiv.org/abs/2408.05127, 2024.